Journal for ImmunoTherapy of Cancer

CLEC2B-KLRB1 axis acts as an immune checkpoint, governing the exhaustion of CD8$^+$ T cells and their resistance to immune checkpoint blockade

Jie Cheng ,[1,2] Jiahua Lu,[1,2] Zhaoya Gao,[3,4] Yifeng Xiao,[5] Pengju Chen,[6] Mengting Zhou,[1,2] Dandan Huang,[3,4] Zihao Zhao ,[7] Xiaohui Zhang,[8] Yuan Zhao,[9] Ming Li,[3,4] Jin Gu[3,4,10,11,12]

To cite: Cheng J, Lu J, Gao Z, *et al*. CLEC2B-KLRB1 axis acts as an immune checkpoint, governing the exhaustion of CD8$^+$ T cells and their resistance to immune checkpoint blockade. *Journal for ImmunoTherapy of Cancer* 2026;**14**:e013637. doi:10.1136/jitc-2025-013637

► Additional supplemental material is published online only. To view, please visit the journal online (https://doi.org/10.1136/jitc-2025-013637).

JC, JL, ZG, YX and PC contributed equally.

Accepted 30 April 2026

For numbered affiliations see end of article.

Correspondence to
Dr Jie Cheng;
jiecheng2024@hust.edu.cn

Professor Ming Li;
limingmd@126.com

Professor Jin Gu;
zlgujin@126.com

ABSTRACT

Background Many patients with cancer benefit little from immune checkpoint blockade (ICB), a major obstacle to immunotherapy for decades. Finding alternative immune checkpoints that control CD8$^+$ T-cell exhaustion is urgent if we are to improve the efficacy of immunotherapies, particularly in microsatellite stable (MSS) colorectal cancer (CRC) that is resistant to ICB.

Methods Spatial proximity is essential for suppressive ligand-receptor signaling. Here, we mapped the spatial tumor microenvironment of patients with MSS CRC at single-cell resolution and analyzed the cells interacting with exhausted CD8$^+$ T cells to identify immune checkpoint ligand-receptor pairs. To investigate the function of this previously unrecognized immune checkpoint, we performed validation studies spanning cellular experiments, mouse models, and clinical patient samples.

Results We found that a subset of MSS CRC exhibits substantial CD8$^+$ T-cell infiltration, but their function is suppressed. We identified CLEC2B (ligand)-KLRB1 (receptor) as a novel inhibiting ligand-receptor pair for CD8$^+$ T cells. KLRB1 acts as an immune checkpoint receptor, increasing CD8$^+$ T-cell exhaustion and facilitating immune escape in various human cancers. Binding of CLEC2B to KLRB1 initiates immunosuppressive signaling in CD8$^+$ T cells. Clinically, CLEC2B-KLRB1 expression correlates positively with cancer progression and poor response to ICB, demonstrating that KLRB1$^+$ CD8$^+$ T cells are a key marker of the poorly responsive ICB subtype. Furthermore, blocking CLEC2B-KLRB1 signaling with antibodies enhances the antitumor function of CD8$^+$ T cells, providing a potential immunotherapy target for ICB non-responders.

Conclusions Our study revealed CLEC2B-KLRB1 as a previously unrecognized immune checkpoint axis that drives T-cell exhaustion specifically in ICB poor responsive MSS CRC. Blockade of KLRB1 with a therapeutic antibody reinvigorated CD8$^+$ T-cell antitumor immunity, positioning this axis as a promising target for enhancing immunotherapy efficiency in malignancies, including CRC and other ICB-resistant cancers.

WHAT IS ALREADY KNOWN ON THIS TOPIC

⇒ The majority of microsatellite instability-high (MSI-H) colorectal cancers (CRCs) respond to immune checkpoint blockade (ICB), whereas microsatellite stable (MSS) CRCs remain largely refractory, highlighting a critical unmet clinical need.

WHAT THIS STUDY ADDS

⇒ In this study, we revealed that a subset of MSS CRCs is characterized by substantial CD8$^+$ T-cell infiltration that is functionally suppressed, rather than an immune-desert phenotype. We identify CLEC2B-KLRB1 as a previously unrecognized immune checkpoint mediating this suppression.

HOW THIS STUDY MIGHT AFFECT RESEARCH, PRACTICE OR POLICY

⇒ Our work thus identified a new therapeutic target for MSS CRC and presents a paradigm for immune checkpoint discovery applicable to other ICB-resistant malignancies.

INTRODUCTION

In the past decade, immunotherapy, especially immune checkpoint blockade (ICB), has revolutionized tumor treatment in many types of solid tumors. However, many patients respond poorly to current therapies, especially microsatellite stable (MSS) colorectal cancer (CRC). Mismatch repair-proficient (MMRp) or MSS CRC constitutes the majority of patients with CRC (up to 80%–90%), with mismatch repair-deficient (MMRd) or microsatellite instability-high (MSI-H) CRC accounting for the remaining 10%–20%.[1] Therefore, the development of effective treatment for MSS CRC is critical for CRC disease. Due to the remarkable success in MSI-H CRC, ICB received approval from the US Food and Drug Administration in 2017 for MSI-H CRC.[2] In contrast, patients with MSS CRC respond poorly to ICB treatment alone,

which becomes one major obstacle for CRC treatment. In addition, ICB has not achieved an effective response in many patients, such as glioblastoma and pancreatic cancer.[3] Hence, the development of more effective ICB targets for MSS CRC as well as other non-responsive patients is urgent for cancer treatment.

An in-depth understanding of the immune evasion mechanism is critical for expanding the benefits of ICB to non-responsive patients. The key distinguishing feature between MSS and MSI-H CRC is tumor mutation burden (TMB).[4] MSI-H CRCs have high TMB caused by defective DNA mismatch repair (MMR), while MSS CRC tumors are MMRp with low TMB. This high TMB is accompanied by high immune cell infiltration, especially T cells, while MSS CRCs show much lower immune cell infiltration. Traditionally, low TMB in MSS CRC, which generates fewer neoantigens, is thought to be the leading reason for scarce T-cell infiltration, causing insufficient T cells to respond to ICB.[3 5] Nevertheless, single-cell analysis across pan-cancer revealed that, although lower than MSI-H CRC, $CD8^+$ T-cell infiltration in some MSS CRCs is higher than many other ICB-responsive patients (Extended Data figure 1a). Indeed, high proportions of exhausted $CD8^+$ T cells exist in many patients with MSS CRC.[6] Hence, $CD8^+$ T cells can recognize neoantigens and differentiate into an exhaustion state, implying that low TMB alone cannot explain the lack of response to ICB treatment in MSS CRC. Herein, we hypothesized that there exist alternative factors that drive exhaustion and dysfunction of $CD8^+$ T cells, leading to immune evasion and non-response to classic ICB targets.

In response to cancer and pathogens, immune system activates to clear antigens, while concurrently regulatory mechanisms are induced to prevent excessive immune activity (tolerance).[7] Unfortunately, many diseases amplify this tolerance program to escape immunity. Notably, inhibitory checkpoint molecules are upregulated to restrain effector functions of $CD8^+$ T cells in patients with cancer, leading to immune evasion and cancer progression.[8 9] Many inhibitory checkpoints belong to receptors expressed on membranes of $CD8^+$ T cells with ligands expressed by cells proximal to receptors. This spatial proximity enables their ligation and transduces inhibitory signals, leading to dysfunction of $CD8^+$ T cells, such as programmed cell death protein 1 (PD-1) and programmed death-ligand 1. By blocking these inhibitory ligand-receptor pairs, ICB therapy has been developed to reinforce antitumor function of $CD8^+$ T cells.[10] However, targeting the classic ligand-receptor pairs has shown few benefits for patients with MSS CRC. The high exhaustion levels in MSS tumor-infiltrating $CD8^+$ T cells imply there exist alternative ligand-receptor pairs which induce exhaustion program to evade classic targeting.

Screen for inhibitory ligand-receptor pairs has drawn much attention in cancer biology, developing from RNAi screening to CRISPR screening.[9 11–13] Nonetheless, screening in vitro or in mouse models overlooked the clinical characteristics of ICB evasion. In addition, the transduction of inhibitory signals depends on proximity and ligation of ligand-receptor pairs, which requires spatial information to detect. However, spatial proximity of ligand-receptor pairs has not been considered in previous studies. In this work, we spatially resolved the microenvironment of $CD8^+$ T cells in patients with MSS CRC. Systematic analysis of ligand-receptor pairs on exhausted $CD8^+$ T cells and their interacting cells identified CLEC2B (ligand)-KLRB1 (receptor) as a potential biomarker for ICB evasion. Functional studies revealed KLRB1 is an inhibitory receptor that drives exhaustion of $CD8^+$ T cells. Binding to the ligand, CLEC2B, initiated this exhaustion signaling. Notably, treatment with anti-KLRB1 efficiently blocked exhaustion and led to enhanced antitumor function, providing potential treatment target for patients with MSS CRC as well as other ICB poor responsive patients.

RESULTS

Substantial $CD8^+$ T-cell infiltration but functional suppression in a subset of MSS CRC

Based on T-cell infiltration and functional status, the tumor microenvironment (TME) can be classified into three types: immune-inflamed (high infiltration with functional activity), immune-excluded (high infiltration but suppressed function), and immune-desert (low infiltration).[14 15] To characterize the T-cell landscape in MSS CRC, we analyzed public single-cell transcriptomic data (figure 1a). Using the median $CD8^+$ T-cell proportion in "hot" MSI-H CRC (10%) as a threshold, we identified a subset of MSS CRC with high $CD8^+$ T-cell infiltration (>10%), a finding validated in an independent public dataset (figure 1b). By collecting MSS CRC tumors from patients, two independent flow cytometry staining protocols (figure 1c and Extended Data online supplemental figure 1b–c) and immunohistochemistry (figure 1d) were used for analysis of $CD8^+$ T-cell infiltration. These results confirmed that a subset of MSS CRC indeed exhibits high $CD8^+$ T-cell infiltration (>10%). Cross-tumor comparative single-cell analysis further revealed that this MSS CRC subset harbors even higher $CD8^+$ T-cell infiltration than some ICB-responsive patients (Extended Data online supplemental figure 1a). Together, these findings challenge the conventional view that MSS tumors are uniformly immune-desert and demonstrate that a subset of MSS patients exhibits a high-infiltration phenotype.

To investigate the status of $CD8^+$ T cells in this subset of patients with MSS CRC, we identified 11 highly infiltrated samples from a total of 14 MSS CRC specimens (figure 1e–f and online supplemental table 1). From these, we performed $CD45^+$ immune cell enrichment combined with unsorted cell admixtures on nine fresh MSS CRC tumor samples for single-cell RNA sequencing (scRNA-seq). High-quality single cells were obtained after stringent quality control. To identify major cell types, we used unsupervised clustering to get 34 clusters and annotated them with classical marker genes (figure 1g and

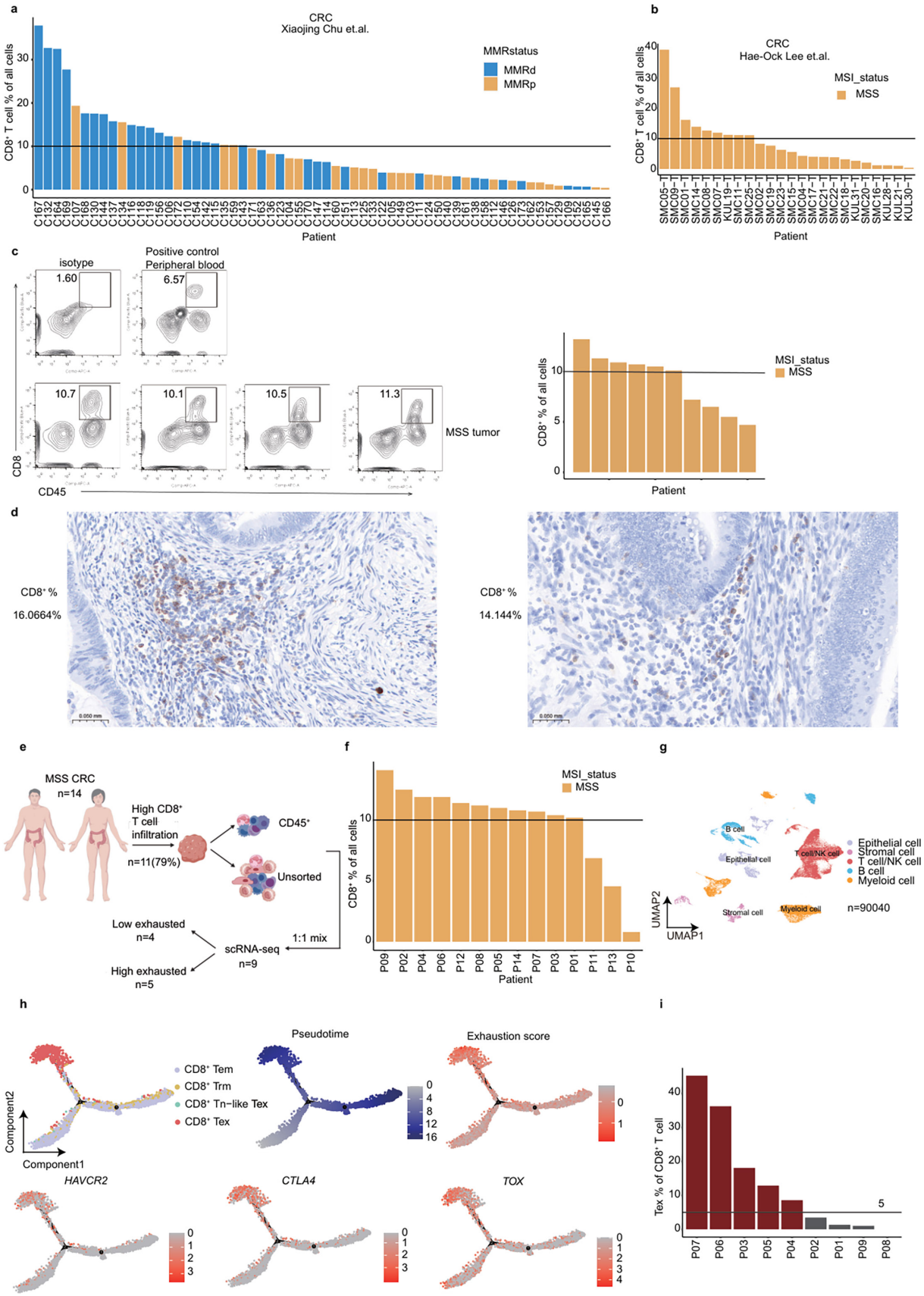

Figure 1 CD8+ T-cell infiltration and state in MSS CRC. (a) CD8+ T cells infiltration in CRCs. scRNA-seq datasets are from Chu *et al*.[19] (b) CD8+ T cells infiltration in patients with MSS CRC. scRNA-seq dataset was from Lee *et al*.[60] (c) CD8+ T cells infiltration in MSS CRCs detected by FACS. The isotype was used as a negative control, and peripheral blood as a positive control.

Figure 1 (Continued)

(d) CD8+ T cells infiltration in MSS CRCs detected by immunohistochemistry. The percentage of CD8-positive cells is indicated beside each plot. Nuclei were stained with hematoxylin, and CD8α was stained with horseradish peroxidase-labeled antibodies and 3,3'-diaminobenzidine. Scale bar=50 µm. (e) Sample and data collection strategy. Figure was created with BioGDP.com.[88] Tumors of MSS CRC were collected and digested into single cells and analyzed by FACS analysis. The samples with high CD8+ T-cell infiltration were enrolled for further sequencing. CD45+ cells were sorted and mixed with unsorted cells for single-cell RNA-sequencing. (f) CD8+ T-cell infiltration in each sample. Tumors of MSS CRC were collected and digested into single cells and analyzed by FACS analysis. High infiltration refers to CD8+ T-cell proportion more than 10%. (g) UMAP plot of 90,040 cells and clusters were colored by major cell types. scRNA-seq data were generated in house. (h) Differentiation trajectory of classic CD8+ T cells. scRNA-seq data were generated in house. Cell subset annotation, pseudotime, exhaustion score and exhaustion genes expression are shown in the trajectory. (i) CD8+ Tex proportion in all CD8+ T cells (including MAIT and IEL). scRNA-seq data were generated in house. High exhausted group with proportion more than 5% is colored red while low exhausted group is colored by gray. CRC, colorectal cancer; FACS, fluorescence activated cell sorter; IEL, intraepithelial lymphocyte; MAIT, mucosal-associated invariant T cell; MMR, mismatch repair; MMRd, mismatch repair-deficient; MMRp, mismatch repair-proficient; MSI-H,microsatellite instability-high; MSS, microsatellite stable; NK, natural killer; scRNA-seq, single-cell RNA sequencing; Tem, effector memory T cell; Tex, exhausted T cell; Tn-like Tex, naïve-like exhausted T cell; Trm, resident memory T cell; UMAP, Uniform Manifold Approximation and Projection.

Extended Data online supplemental figure 2a). T/natural killer (NK) cells dominated the immune landscape across samples, while myeloid enrichment characterized P05/P06 and B-cell predominance distinguished P03/P04/P09 (Extended Data online supplemental figure 2b).

Subclustering of major cell types revealed extensive heterogeneity (Extended Data online supplemental figure 2c–g). Specifically, classical CD8+ T cells exhibited four functional states: effector memory (CD8+ Tem), resident memory (CD8+ Trm), Tn-like exhausted (CD8+ Tn-like Tex) and terminally exhausted (CD8+ Tex) (Extended Data online supplemental figure 2h), consistent with previous classifications.[16] Cell trajectory analysis revealed that CD8+ T cells differentiate into exhaustion state with high expression of exhaustion-associated genes and low expression of memory-associated genes (figure 1h and Extended Data online supplemental figure 2i). Among highly infiltrated samples, the median proportion of Tex in MSS CRC showed a trend towards being higher, although not statistically significant (Extended Data online supplemental figure 2j). Strikingly, analysis of the Tex proportion in our data showed that some MSS CRCs had a high proportion of Tex, even up to 40% (figure 1i). Therefore, the high frequency of Tex in some patients with MSS CRC, who nevertheless respond poorly to ICB therapies, prompted us to hypothesize that alternative immune evasion mechanisms may underlie ICB resistance in MSS CRC.

Cell interaction of exhausted CD8+ T cells in TME of MSS colorectal cancer

Cell interactions provide potential escaping factors for regulating exhausted CD8+ T cells in TME. Cell interactions require proximity while single-cell sequencing cannot provide spatial information, so we studied spatial interactions of exhausted CD8+ T cells in TME by analyzing spatial transcriptomic sequencing data. Publicly available spatial transcriptomic datasets from 18 MSS CRC samples were collected and analyzed. To resolve the TME architecture at single-cell resolution, we applied cell2location[17] to deconvolute spatial spots and quantify subset-specific densities. Density and signature score correlation[18] identified immune subsets that were spatially proximal to CD8+ Tex (figure 2a–b). Furthermore, we validated cell interactions by using scRNA-seq. scRNA-seq data were divided into high and low exhausted groups (figure 1i), and Ro/e score[19] was calculated to identify cell subsets enriched in the high exhausted group (figure 2c). Critically, after the combination of spatial data and single-cell data, four subsets (intraepithelial lymphocyte (IEL)-like natural killer T cell (NKT), CD4+ Tn, CD4+ Tn-like regulatory T cell (Treg) and *C1QC*+ Mac) stood out as the most correlated interacting cells of Tex (figure 2d, Extended Data online supplemental figure 3a). Consistent with previous studies, the known T-cell suppressive cells Treg and *C1QC*+ Mac[20–22] were correlated with Tex. Notably, IEL-like NKT and CD4+ Tn showed a high correlation coefficient with CD8+ Tex (Extended Data online supplemental figure 3b). In general, by the combination of spatial co-localization and proportion correlation analyses, four subsets were identified as potential interacting cells in the microenvironment of CD8+ Tex. A particularly noteworthy correlation was identified between CD4+ Tn-like Treg and exhausted CD8+ T cells, as revealed by the analysis of flow cytometry (figure 2e).

Then we screened for immune checkpoints by analyzing ligand-receptor pairs in CD8+ Tex and four interacting cells with CellChat.[23] Systematic analysis revealed *C1QC*+ macrophages acted as the dominant signal source toward CD8+ Tex (Extended Data online supplemental figure 3c). Pathway-level interrogation identified conserved MHC-I, CLEC and MIF signal modules across all subsets (Extended Data online supplemental figure 3d). Ligand-receptor pairs analysis revealed that the known inhibitory pairs *NECTIN2-TIGIT*,[24 25] *LGALS9-HAVCR2*[26–28] and *CD80/CD86-CTLA4*[27 28] existed in *C1QC*+ Mac and CD8+ Tex, and *CLEC2D-KLRB1*[29] existed in IEL-like NKT, CD4+ Tn, CD4+ Tn-like Treg and CD8+ Tex (figure 2f). Consistently, after checking the known inhibitor ligands and receptors[24–28 30] (online supplemental table 2), the same interactions were identified.

To search for functional receptors in Tex, we correlated the expression of receptors with T-pcell exhaustion score

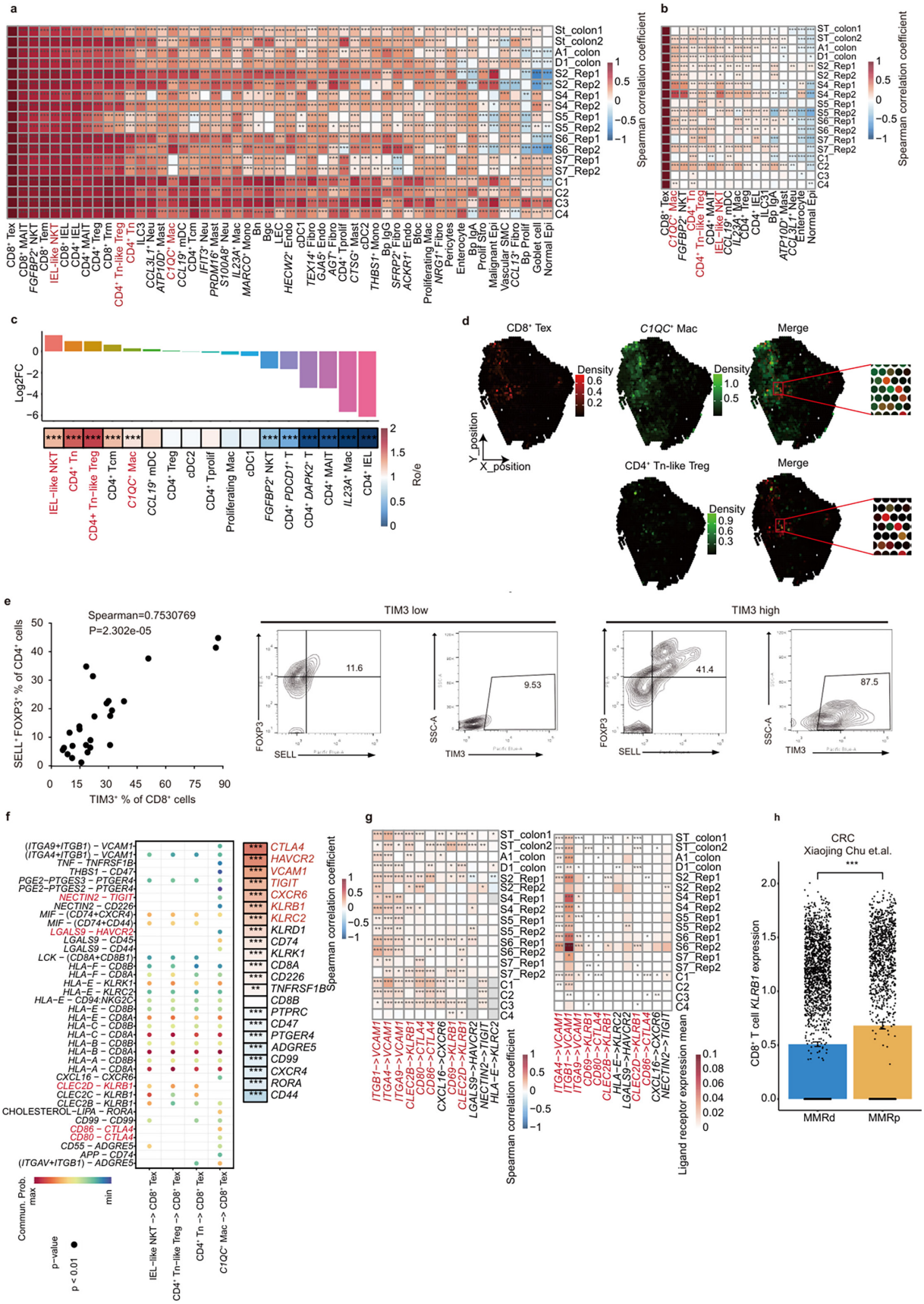

Figure 2 Interaction between CD8⁺ Tex and four subsets. (a) Heatmap of Spearman correlation coefficient between CD8⁺ Tex density and all subsets density in public spatial transcriptome data.[63 67–69] The column is ordered by mean Spearman correlation coefficient. Four CD8⁺ Tex-associated subsets are highlighted in red. The Benjamini-Hochberg method was used for multiple

Figure 2 (Continued)

testing correction. *p<0.05, **p<0.01, ***p<0.001. (b) Heatmap of Spearman correlation coefficient between CD8+ Tex signature score and subsets signature score in public spatial transcriptome data.[63 67–69] All the subsets with mean Spearman correlation coefficient more than 0.4 in a were selected to show. Three subsets (Bp IgA, enterocyte and normal Epi) were chosen as negative control. The column is ordered by mean Spearman correlation coefficient. Four CD8+ Tex-associated subsets are highlighted in red. The Benjamini-Hochberg method was used for multiple testing correction. *p<0.05, **p<0.01, ***p<0.001. (c) Cell enrichment at group level of in-house scRNA-seq data. NKT cells, CD4+ T cells and macrophage lineages were shown. Top, $\log_2$ fold change (high exhausted group vs low exhausted group) of subset's proportion. Bottom, ratio of observed cell number versus expected cell number (Ro/e) of each subset. Statistical significance was assessed using χ^2 test. ***p<0.001. (d) Co-localization visualization in spatial transcriptome data of S6_Rep2 sample.[67] (e) Tumors of MSS CRC were collected and digested into single cells and analyzed by FACS analysis. Left panel, correlation between the percentage of TIM3+ CD8+ T cells and SELL+ FOXP3+ CD4+ T cells. Each dot represents a sample (n=25). P value was calculated by Spearman correlation analysis. Middle and right panels, gating of TIM3+ CD8+ T cell and SELL+ FOXP3+ CD4+ T-cell populations. (f) Interaction analysis of in-house scRNA-seq data. Left, ligand-receptor pairs identified by CellChat between CD8+ Tex and four CD8+ Tex-associated subsets. Only incoming interactions of CD8+ Tex are shown. Known immune suppression interactions are highlighted in red. Right, Spearman correlation coefficient between receptors expression and CD8+ Tex signature scores in classic CD8+ T cells. Candidates of exhaustion-related receptors with Spearman correlation coefficient more than 0.15 are highlighted in red. **p<0.01, ***p<0.001. (g) Co-localization analysis of candidate receptors and corresponding ligands in public spatial transcriptome data.[63 67–69] Left, heatmap of Spearman correlation coefficient between receptor's expression and ligand's expression. The column is ordered by mean Spearman correlation coefficient. Gray box means Spearman correlation coefficient is unavailable. *p<0.05, **p<0.01, ***p<0.001. Right, heatmap of the mean product of receptor and ligand. The column is ordered by mean product. Statistical significance was assessed using permutation test. *p<0.05, **p<0.01, *** p<0.001. (h) *KLRB1* expression in patients with MMRd and MMRp CRC. scRNA-seq data are from Chu *et al*.[19] Only classic CD8+ T cells are included. Statistical significance was assessed using a two-sided unpaired Student's t-test with heteroscedasticity. ***p<0.001. CRC, colorectal cancer; cDC, classic dendritic cell; FACS, fluorescence activated cell sorter; FC, fold change; IEL, intraepithelial lymphocyte; MAIT, mucosal-associated invariant T cell; mDC, myeloid dendritic cell; MMRd, mismatch repair-deficient; MMRp, mismatch repair-proficient; MSS, microsatellite stable; NKT, natural killer T cell; scRNA-seq, single-cell RNA sequencing; Tcm, central memory T cell; Tem, effector memory T cell; Tex, exhausted T cell; Tn-like Tex, naïve-like exhausted T cell; Treg, regulatory T cell; Trm, resident memory T cell.

and seven candidates were identified (figure 2f). Consistently, three canonical immune checkpoint receptors (*CTLA4*, *HAVCR2*, *TIGIT*) showed significant correlation (figure 2f). Next we analyzed the ligands for these inhibitor receptors. Since co-occurrence is basic for spatial interaction of ligand and receptor,[31] we leveraged spatial correlation analysis and permutation-test based co-localization analysis.[18 32] Critically, eight functionally interacting pairs (*ITGB1/ITGA4/ITGA9-VCAM1*, *CLEC2B/C/D-KLRB1* and *CD80/CD86-CTLA4*) were found (figure 2g). Further, we compared the expression of the three receptors with ICB responsiveness by using patients with MMRd and MMRp CRC. *CTLA4* showed no difference between MMRd and MMRp patients (Extended Data online supplemental figure 3e), consistent with no clinical efficacy of targeting cytotoxic T-lymphocyte associated protein 4 (CTLA4) in MSS CRC.[33] Strikingly, *KLRB1* showed significantly higher expression in MMRp CRC, compared with MMRd patients (figure 2h). On the contrary, *VCAM1* presented reverse expression pattern (Extended Data online supplemental figure 3e). Collectively, these data implied that KLRB1 may be the potential factor driving immune evasion in MSS CRC.

KLRB1 is an exhaustion marker on CD8+ T cells in poor responsive patients

KLRB1 is a classic marker for NK cells,[34] but whether patients with KLRB1+ CD8+ T cells represent a subtype of MSS CRC is unknown. By analyzing scRNA-seq data as well as protein expression by fluorescence activated cell sorter (FACS) analysis, we found KLRB1+CD8+ T cells account for a large proportion of CD8+ T cells (>20%) in more than 90% of patients with MSS CRC (figure 3a–b). This phenomenon was further validated in other types of cancer (figure 3c). These results indicated that high expression of KLRB1 on CD8+ T cells represents a large subtype of patients with cancer.

Next we explored the correlation between KLRB1 and exhaustion by conducting a comprehensive pan-cancer analysis. At the bulk level, correlation between exhaustion score and *KLRB1* was significantly high (figure 3d). Critically, significant positive correlations between *KLRB1* expression and the exhaustion score across multiple cancer types were unveiled at single-cell level (figure 3e). Interestingly, exhaustion score in CRC positively correlated with *KLRB1*. Although the correlation score in CRC was not the highest, this implies that not only in CRC, this immune evasion associated with KLRB1 may exist in many other types of cancer. Since uterine corpus endometrial carcinoma, lung cancer and pancreatic cancer showed the highest correlation with *KLRB1*, we used these top three cancer types for further analysis. Detailed subset study showed *KLRB1* is highly expressed in exhausted T cells (CD8.c11.Tex.*PDCD1*, CD8.c12.Tex.*CXCL13*, CD8.c13.Tex.*MYL12A* and CD8.c14.Tex.*TCF7*), accompanied by high levels of Tex marker genes (Extended Data online supplemental figure 4a–b). Uniform Manifold Approximation and Projection (UMAP) plot revealed that exhausted cells showed high expression level of *KLRB1* (Extended Data online supplemental figure 4c). Furthermore, *KLRB1*^{high}

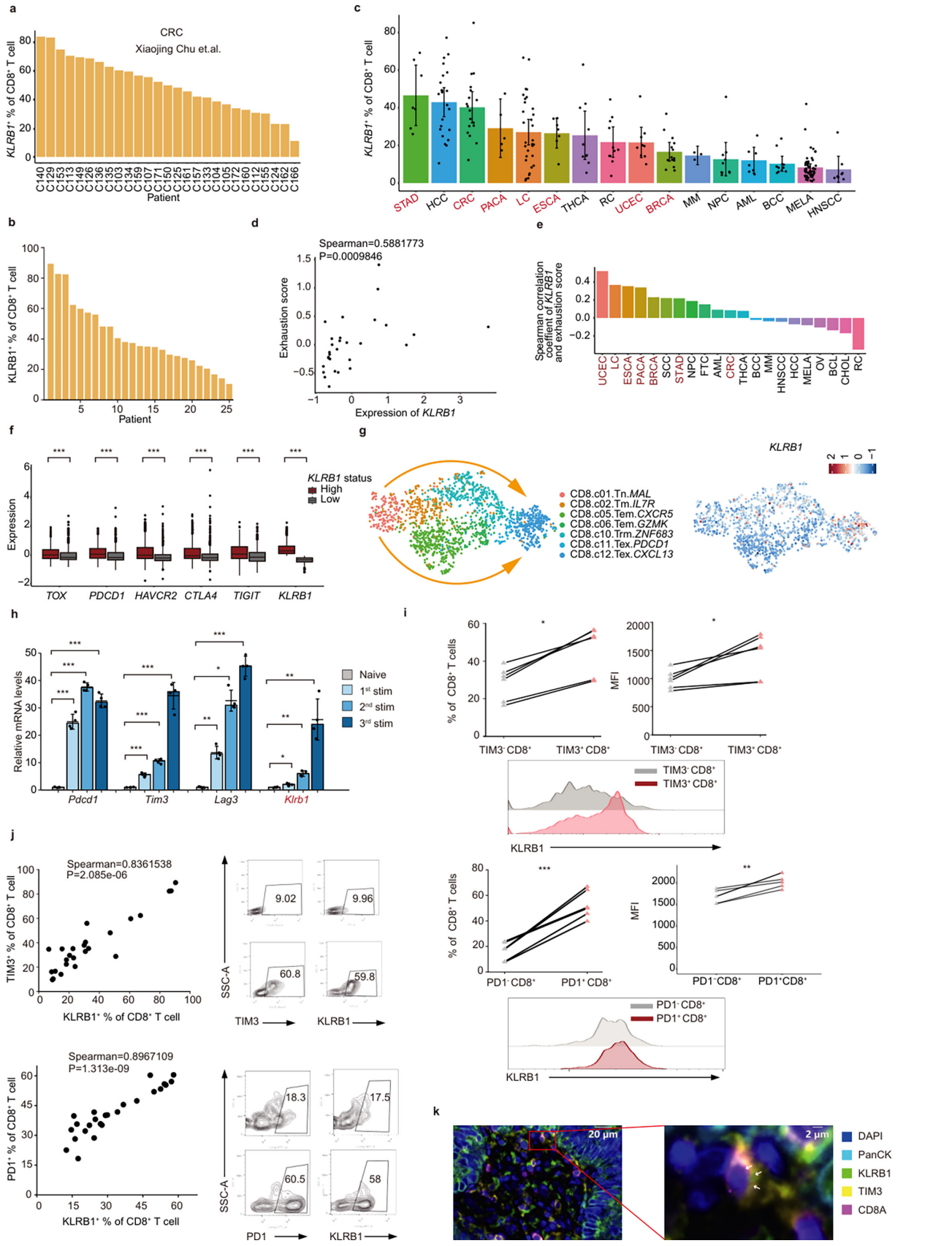

Figure 3 Correlation between KLRB1 and exhaustion. (a) *KLRB1*$^+$ CD8$^+$ T-cell proportion in patients with MMRp CRC. scRNA-seq data are from Chu *et al*.[19] Only classic CD8$^+$ T cells are included. (b) Tumors of MSS CRC were collected and digested into single cells and analyzed by FACS analysis. KLRB1$^+$ CD8$^+$ T-cell proportions in patients with MSS CRC are shown. (c) *KLRB1*$^+$ CD8$^+$ T-cell proportion in patients with pan-cancer. scRNA-seq data are from Zheng *et al*.[78] Only classic CD8$^+$ T cells are

Figure 3 (Continued)

included. Bars represent the mean values, and error bars represent the 95% CIs. Each dot represents a sample. (d) Correlation between *KLRB1* and exhaustion score in bulk RNA-seq data. Bulk RNA-seq data are from Zheng *et al*.[78] (e) Correlation between *KLRB1* and exhaustion score of pan-cancer CD8$^+$ T cells. scRNA-seq data are from Zheng *et al*.[78] Only classic CD8$^+$ T cells are included. (f) Expression of exhaustion genes in *KLRB1* high and low groups. scRNA-seq data are from Zheng *et al*.[78] Only classic CD8$^+$ T cells are included. Each dot represents a cell. Statistical significance was assessed using two-sided unpaired Student's t-test with heteroscedasticity. ***p<0.001. (g) *KLRB1* expression in differentiation trajectory. scRNA-seq data are from Zheng *et al*.[78] (h) Mouse naive CD8$^+$ T cells enriched from spleen were stimulated with anti-CD3 (3.5 µg/mL) and CD28 (1 µg/mL) antibodies three times every 2 days or not (naive). mRNA levels were analyzed on day 0, 2, 4, and 6 and determined by RT-PCR (n=4 independent wells). Bars represent the median values; data are the mean±SD. ***p<0.001 by two-sided unpaired Student's t-test with heteroscedasticity. In the *Lag-3* group, the data from the second stimulation were not normally distributed; therefore, the Wilcoxon test was used. (i) Percentage and MFI of KLRB1 expression in mouse CRC tumor-infiltrated TIM3$^-$/PD-1$^-$ and TIM3$^+$/PD-1$^+$ CD8$^+$ T cells. C57BL/6 mice injected subcutaneously MC38-OVA cells were immunodepleted by irradiation (2.5 Gy, two times). Naive OT-I CD8$^+$ T cells were stimulated with $OVA_{257–264}$ peptide and adoptively transferred by tail vein injection (intravenous). After 14 days, tumor-infiltrated CD8$^+$ T cells were measured by FACS. Each triangle dot represents a sample (n=6). P value was calculated by two-sided paired Student's t-test. In the TIM3$^+$CD8$^+$ group, the percentage data were not normally distributed; therefore, the paired Wilcoxon test was used. *p<0.05, **p<0.01, ***p<0.001. (j) Tumors of patients with MSS CRC were collected and digested into single cells and analyzed by FACS analysis. Left panel, correlation between the percentage of TIM3/PD-1 and KLRB1 in CD8$^+$ T cells in patients with MSS CRC samples. Each dot represents a sample (n=25). P value was calculated by Spearman correlation analysis. Right panels, population of TIM3$^+$/PD-1$^+$ or KLRB1$^+$ in CD8$^+$ T cells. (k) Patients with MSS CRC tumor section was subjected to multiplex immunohistochemistry for DAPI, PanCK, KLRB1, TIM3 and CD8A. Bar, 20 µm and 2 µm. AML, acute myeloid leukemia; BCL, B cell lymphoma; BRCA, breast cancer; CHOL, cholangiocarcinoma; CRC, colorectal cancer; ESCA, esophageal carcinoma; FACS, fluorescence activated cell sorter; FTC, follicular thyroid carcinoma; HNSCC, head and neck squamous cell carcinoma; LC, lung cancer; MELA, melanoma; MFI, mean fluorescence intensity; MM, multiple myeloma; MMRp, mismatch repair-proficient; MSS, microsatellite stable; mRNA, messenger RNA; NPC, nasopharyngeal carcinoma; OV, ovarian serous cystadenocarcinoma; PACA, pancreatic cancer; PD-1, programmed cell death protein 1; RC, rectal cancer; RNA-seq, RNA sequencing; RT-PCR, reverse transcription-polymerase chain reaction; SCC, squamous cell carcinoma; scRNA-seq, single-cell RNA sequencing; STAD, stomach adenocarcinoma; THCA, thyroid carcinoma; TIM3, T-cell immunoglobulin and mucin-domain containing molecule 3; UCEC, uterine corpus endometrial carcinoma.

CD8$^+$ T cells exhibited elevated expression of canonical exhaustion-associated genes (figure 3f). We then systematically analyzed the differentiation trajectory of CD8$^+$ T cells. During terminal differentiation trajectory, *KLRB1*$^+$ cells are enriched in the Tex cells rather than in naive cells (figure 3g).

Then we confirmed the expression pattern of KLRB1 in an in vitro terminal differentiation model. Chronic T-cell receptor (TCR) signaling for terminal differentiation was induced in mouse primary CD8$^+$ T cells by continuous anti-CD3 and anti-CD28 antibodies stimulation, as previously reported.[35] It was observed that both the messenger RNA (mRNA) and protein levels of KLRB1 exhibited a gradual increase during the course of terminal exhaustion, in consistent with the established immune checkpoint receptors PD-1, T-cell immunoglobulin and mucin-domain containing molecule 3 (TIM3) and lymphocyte activation gene 3 (LAG-3) (figure 3h and Extended Data online supplemental figure 4d). In addition, in mouse colon cancer and melanoma, tumor-infiltrated CD8$^+$ T cells showed KLRB1 expression in TIM3$^+$CD8$^+$ T cells were significantly higher compared with TIM3$^-$CD8$^+$ T cells (figure 3i and Extended Data online supplemental figure 8a). Similarly, KLRB1 expression in PD-1$^+$CD8$^+$ T cells was also significantly higher compared with PD-1$^-$CD8$^+$ T cells (figure 3i and Extended Data online supplemental figure 8a). We also extended this analysis to patients with MSS CRC. Consistent with mouse data, KLRB1 was positively correlated with TIM3 and PD-1 in CD8$^+$ T cells (figure 3j). In addition, *KLRB1* was positively correlated with classic exhaustion markers in public bulk RNA sequencing (RNA-seq) data of the cancer genome atlas (TCGA) CRC cohort (Extended Data online supplemental figure 4e). Immunofluorescence assays demonstrated the expression of KLRB1 in exhausted CD8$^+$ T cells (figure 3k). Collectively, both patient data and mouse data identified KLRB1 as an exhaustion marker for CD8$^+$ T cells.

KLRB1 is an immune checkpoint receptor that directing exhaustion of CD8$^+$ T cells

The functions of KLRB1 have been focused on NK cells,[36] but rarely in CD8$^+$ T cells. So next we set out to investigate the role of KLRB1 in CD8$^+$ T cell. KLRB1 was overexpressed or knocked down in mouse and human primary CD8$^+$ T cells (Extended Data online supplemental figure 5a and figure 4a). Remarkably, elevated expression levels of exhaustion-related genes were observed in the overexpression group, while the downregulation of KLRB1 led to a reduction of exhaustion (Extended Data online supplemental figure 5b and figure 4b–c). Consequently, the introduction of KLRB1 led to the suppression of cytokines and KI67 expression (Extended Data online supplemental figure 5c–d and figure 4d), as well as cancer cell killing (Extended Data online supplemental figure 5e and figure 4e) and T-cell proliferation (Extended Data online supplemental figure 5f and figure 4f), while the knockdown of KLRB1 had opposite effects.

Then we studied the function of KLRB1 in mouse colon cancer. Overexpression of KLRB1 significantly promoted tumor size and tumor weight, while deletion of KLRB1

decreased tumor progression (figure 4g–h). Detailed analysis showed the percentage of tumor-infiltrated CD8$^+$ T cells was inhibited by KLRB1 (figure 4i). The expression of exhaustion markers and cell death were enhanced by KLRB1, while cytokines and proliferation were inhibited by KLRB1 (figure 4j–l). The conclusion was further corroborated in a mouse model of melanoma (Extended Data online supplemental figure 5g–j). Consistent with mouse data, in patients with MSS colorectal, *KLRB1*$^+$ CD8$^+$ T cells exhibited exhaustion characteristics, including attenuated immune response activation pathways (*PLCL1*,[37] *RASA3*[38]), downregulation of cytotoxic effector molecules, and overexpression of exhaustion-associated markers (figure 4m–n). Interestingly, *CCL20*, which was reported to recruit Treg,[39] was highly expressed in *KLRB1*$^+$ CD8$^+$ T cells (figure 4m–n). Together, these data revealed that KLRB1 serves as an immune checkpoint receptor triggering exhaustion and dysfunction in CD8$^+$ T cells.

CLEC2B-KLRB1 interaction elicits suppressive signaling in CD8$^+$ T cells

Then we set out to explore the mechanism of KLRB1 regulation. Specific ligand-receptor interaction leads to transmission of signals into CD8$^+$ T cells and determines the fate of cells. Therefore, we set out to explore the ligands of KLRB1. There are three known ligands for KLRB1, CLEC2B/C/D in CellChat database[23] (figure 2f). To identify the key ligand interaction for ICB response, we investigated their expression in high exhausted group and correlation with ICB response. Notably, among these candidates, only *CLEC2B* exhibited higher expression level in high exhausted group's CD4$^+$ Tn-like Treg and showing the most significant negative correlation with favorable ICB responses (figure 5a–b). Despite higher *CLEC2C* expression in IEL-like NKT cells and higher *CLEC2B* expression in *C1QC*$^+$ macrophages in the high exhausted group, evidence linking these specific expression patterns to ICB response is lacking (Extended Data online supplemental figure 6a–b). These results indicated that CLEC2B may be the ligand responsible for exhaustion and ICB non-response. Therefore, we focused on CLEC2B for further studies. Spatial interaction of *CLEC2B-KLRB1* was observed by co-localization analysis of spatial transcriptomic datasets (figure 5c). Critically, Tex-enriched spots had higher expression of *CLEC2B*, validated by statistical analysis (figure 5d).

Then we investigated the interaction of CLEC2B and KLRB1. First, an exogenous interaction test was carried out by using purified FLAG-KLRB1 and HA-CLEC2B proteins. An immunoprecipitation assay was performed using anti-FLAG antibody and HA-CLEC2B was pulled down, proving the binding of exogenous proteins in vitro (figure 5e). Then we tested the binding of endogenous proteins using lysates of exhausted CD8$^+$ T cells and CLEC2B$^+$ CD4$^+$ T cells sorted from patients with MSS CRC. Consistently, CLEC2B is immunoprecipitated down by anti-KLRB1 (figure 5e). These results indicated that there exists a direct interaction between KLRB1 on CD8$^+$ T cells and CLEC2B on CD4$^+$ T cells.

Then we studied the downstream signaling of CLEC2B-KLRB1 in CD8$^+$ T cells. KLRB1 is a transmembrane receptor that exhibits both activating and inhibitory functions in NK cells.[40] Tyrosine phosphorylation is a key mechanism for signal transduction and regulation in the immune system.[41] Therefore, we explored tyrosine phosphorylation of KLRB1 as well as activation of TCR signaling. Notably, CLEC2B binding enhanced levels of tyrosine phosphorylation on KLRB1, both in purified and endogenous proteins (figure 5f). In addition, downstream of TCR signaling, the PI3K-AKT pathway and ERK pathway were suppressed by CLEC2B (figure 5g). Consistently, scRNA-seq data also showed that expression of TCR signaling molecules and activity of TCR downstream transcription factor (TF) (Nuclear Factor of activated T Cells (NFAT)) were downregulated in *KLRB1*$^+$ CD8$^+$ T cells (figure 5h–i). Further analysis demonstrated that CLEC2B could increase mRNA and protein levels of exhaustion markers, which was rescued by treatment with anti-KLRB1 antibody (Extended Data online supplemental figure 6c–d and figure 5k). Collectively, CLEC2B-KLRB1 inhibited activation of TCR signaling through ligand-receptor interaction (figure 5j).

Blockade of KLRB1 enhances antitumor immunity of CD8$^+$ T cells

We further assessed the clinical relevance of CLEC2B-KLRB1. Critically, KLRB1 expression on CD8$^+$ T cells showed a significantly positive correlation with tumor progression in patients with CRC (figure 6a), consistent with the known exhaustion marker, TIM3 (Extended Data online supplemental figure 7a). In addition, CLEC2B expression on CD4$^+$ T cells also exhibited positive correlation with tumor progression in patients with CRC (figure 6b). Further survival analysis observed that patients with CRC with elevated *CLEC2B* or *KLRB1* expression exhibit significantly reduced overall survival and disease-free survival (figure 6c and Extended Data online supplemental figure 7b). This prognostic association was consistent across multiple types of malignancies (Extended Data online supplemental figure 7c). Furthermore, many cancer types with high non-response rates showed a high proportion of *KLRB1*$^+$ CD8$^+$ T cells, which confirmed that high infiltration of *KLRB1*$^+$ CD8$^+$ T cells can represent a category of patients in clinical (figures 3c and 6d). Moreover, high *CLEC2B* levels in CD4$^+$ Tn-like Treg and elevated *KLRB1* expression in classical CD8$^+$ T cells were negatively correlated with ICB response in CRC (figures 2h and 5b). Notably, not only in CRC but also in hepatocellular carcinoma (HCC), triple-negative breast cancer and head and neck squamous cell carcinoma, their expression showed a negative correlation with ICB response (figure 6e).

Then we assessed the antitumor effect of KLRB1 blockade in mouse models. Colon cancer-bearing C57BL/6 mice infused with OVA peptide-primed

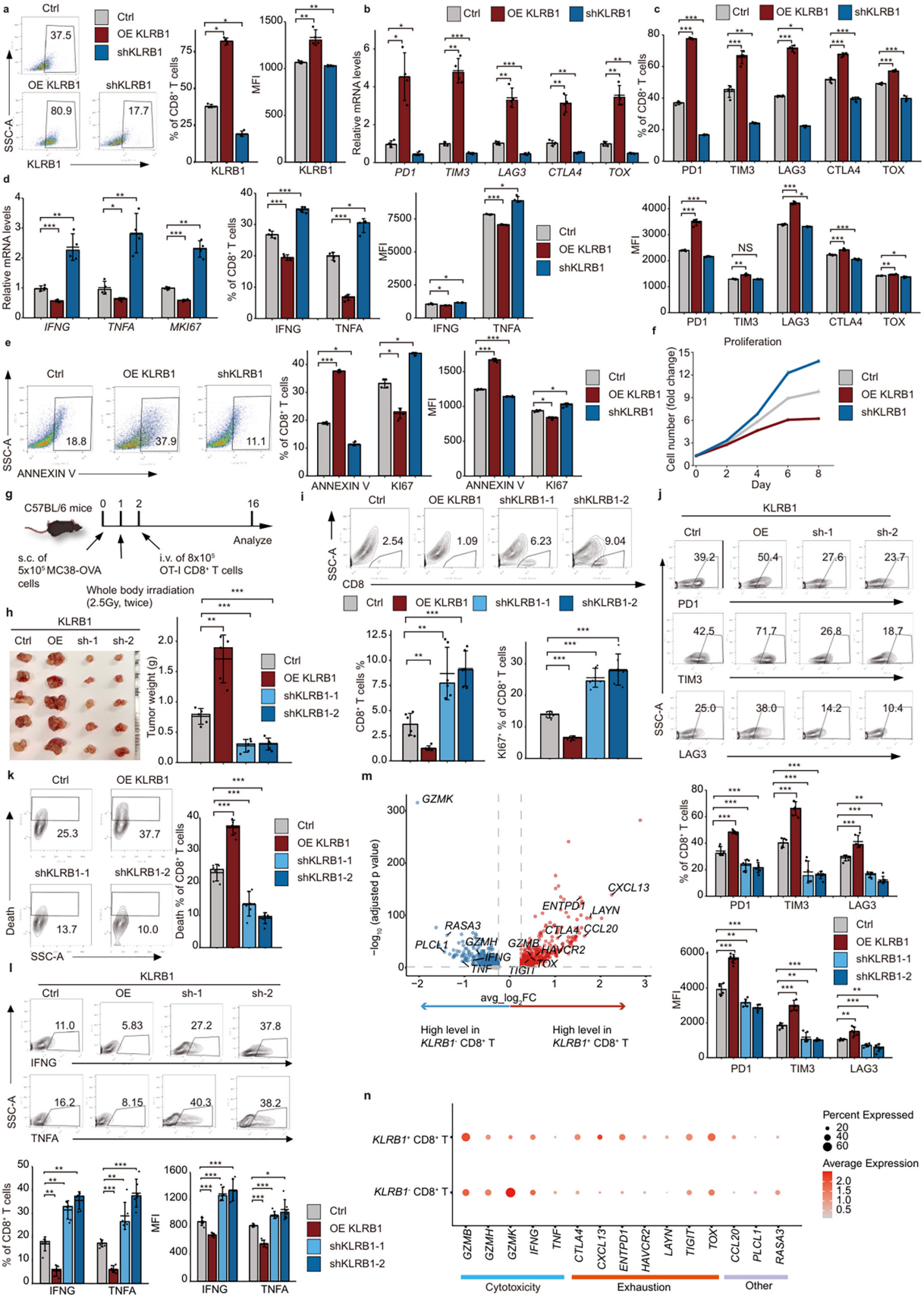

Figure 4 Exhaustion induced by KLBR1. (a–f) Human naive CD8⁺ T cells enriched from PBMC were stimulated with anti-CD3/CD28 antibodies (n=4 per group). Then KLRB1 was overexpressed or knocked down. After another three times' stimulation, the expression of KLRB1 (a) was analyzed by FACS. mRNA and protein levels of exhaustion genes (b–c) were analyzed by RT-

Figure 4 (Continued)

qPCR and FACS. mRNA and protein levels of cytokines and KI67 (d–e) were analyzed by RT-qPCR and FACS. Annexin V was determined by FACS analysis (e). Cell numbers before each stimulation were counted (f). Bars represent the median values, data are the mean±SD. NS p≥0.05, *p<0.05, **p<0.01, ***p<0.001 by two-sided unpaired Student's t-test with heteroscedasticity. For the proportion of KLRB1-positive cells, the control group data were not normally distributed; for PD-1 mRNA levels, the KLRB1-knockdown group data were not normally distributed; for the proportion of LAG-3-positive cells, the KLRB1-knockdown group data were not normally distributed; for TNF-α mRNA levels, the KLRB1-overexpression group data were not normally distributed; for the proportion of TNF-α-positive cells and its MFI, the KLRB1-knockdown group data were not normally distributed; for the proportion of Annexin V-positive cells, the KLRB1-knockdown group data were not normally distributed; for the proportion of Ki-67-positive cells, the control group data were not normally distributed; and for Ki-67 MFI, both the KLRB1-overexpression and KLRB1-knockdown group data were not normally distributed. The Wilcoxon test was therefore used in all these cases. (g–l) n=6 per group, (h), n=5 per group (g), C57BL/6 mice injected subcutaneously with 5×10^5 MC38-OVA cells were immunodepleted by irradiation (2.5 Gy, two times). Naive OT-I $CD8^+$ T cells were stimulated with $OVA_{257–264}$ peptide for 24 hours and transfected with lentivirus for overexpression or knockdown of KLRB1, vector lentivirus as control. 1 day post irradiation, OT-I $CD8^+$ T cells were adoptively transferred by tail vein injection (i.v.). After 14 days, tumor burden (h) Tumor-infiltrated $CD8^+$ T cells (i), percentage and MFI of exhaustion proteins (j), cell death (7AAD, k) were measured. After stimulated with 50 ng/mL 1 phorbol 12-myristate 13-acetate and ionomycin in the presence of 5 mg/mL 1 Brefeldin A at 37°C for 4 hours, production of cytokines (l) were measured by FACS analysis. Bars represent the median values, data are the mean±SD. *p<0.05, **p<0.01, ***p<0.001 by two-sided unpaired Student's t-test with heteroscedasticity. For the proportion of $CD8^+$ T cells, the KLRB1-overexpression group data were not normally distributed; for the proportion of LAG-3-positive cells, the second KLRB1-knockdown group data were not normally distributed; for the proportion of IFN-γ-positive cells, both the control group and the second KLRB1-knockdown group data were not normally distributed; and for the proportion of TNF-α-positive cells, the first KLRB1-knockdown group data were not normally distributed. The Wilcoxon test was therefore used in all these cases. (g) was created in BioRender. (m) Volcano plot of differentially expressed genes between *KLRB1* positive and negative $CD8^+$ T cells in scRNA-seq data generated in house. Genes with adjusted p value<0.05 and absolute value of avg_log_2FC more than 0.25 were considered as differentially expressed genes. Genes highly expressed in *KLRB1*$^+$ $CD8^+$ T cells are colored red while genes highly expressed in *KLRB1*$^-$ $CD8^+$ T cells are colored blue. Genes with no significant differences are gray. Only classic $CD8^+$ T cells are included. (n) Dot plots of differentially expressed genes labeled in m in scRNA-seq data generated in house. CTLA4, cytotoxic T-lymphocyte associated protein; FACS, fluorescence activated cell sorter; FC, fold change; IFN, interferon; i.v., intravenous; LAG-3, lymphocyte activation gene 3; mRNA, messenger RNA; NS, not significant; PBMC, peripheral blood mononuclear cell; PD-1, programmed cell death protein 1; RT-qPCR, real-time quantitative reverse transcription polymerase chain reaction; scRNA-seq, single-cell RNA sequencing; s.c., subcutaneous injections; TIM3, T-cell immunoglobulin and mucin-domain containing molecule 3; TNF, tumor necrosis factor; TOX, thymocyte selection-associated high mobility group box; 7AAD, 7-aminoactinomycin D.

OT-I $CD8^+$ T cells were used. Then mice were treated with either an anti-KLRB1 antibody or an IgG control (figure 6f). Remarkably, treatment with anti-KLRB1 significantly suppressed the growth of tumors (figure 6f) and increased tumor-infiltrating $CD8^+$ T cells (figure 6g) in C57BL/6 mice, but not in $CD8^+$ T cell-depleted C57BL/6 mice, suggesting that KLRB1 functions in a $CD8^+$ T cell-dependent manner (figure 6f–g). Furthermore, a decline in exhaustion proteins (figure 6h) and an augmentation in cytokine production and KI67 in tumor-infiltrating $CD8^+$ T cells were observed (figure 6i). The conclusion was further corroborated in a mouse model of melanoma (Extended Data online supplemental figure 8b–e). Therefore, KLRB1 serves as an effective target for ICB on $CD8^+$ T cells. In summary, these findings identified that CLEC2B-KLRB1 is a promising marker for ICB resistance and blockade of KLRB1 enhances antitumor immunity of $CD8^+$ T cells (figure 6j).

DISCUSSION

The dominant proportion of MSS in CRC and poor response to ICB therapies make the poor responsiveness to immunotherapy one key hurdle in CRC treatment. Identification of new targets for enhancing the responsiveness of MSS CRC to immunotherapy is an open question in CRC. In this study, we found exhausted $CD8^+$ T cells constitute a large proportion of $CD8^+$ T cells in MSS CRC TME. This phenomenon raised the question regarding the mechanisms that regulate exhaustion and whether these regulations can be targeted for MSS CRC treatment. For mechanistic study, we analyzed the spatial transcriptome of TME to identify ligand-receptor pairs that drive exhaustion of $CD8^+$ T cells. Critically, *CLEC2B-KLRB1* stood out as the ligand-receptor pair correlated with ICB non-responsiveness. Strikingly, *KLRB1* expression on $CD8^+$ T cells is present in a large proportion of patients with cancer and predicts low response to ICB not only in MSS CRC, but also in other types of cancer. Additionally, the frequency of KLRB1$^+$ $CD8^+$ T cells is positively correlated with tumor progression. Therefore, high-level expression of KLRB1 on $CD8^+$ T cells represents a new subtype of MSS CRC which is highly non-responsive to ICB. Clinically, the membrane location of KLRB1 makes it achievable to be targeted by antibodies. We found antibody blockade of KLRB1 effectively enhanced the antitumor function of $CD8^+$ T cells. Together, our study discovered that KLRB1 is an immune checkpoint receptor for exhaustion of $CD8^+$ T cells and targeting KLRB1 with antibodies is a promising treatment for CRC. Further clinical trials are necessary for the application of anti-KLRB1 in MSS CRC treatment.

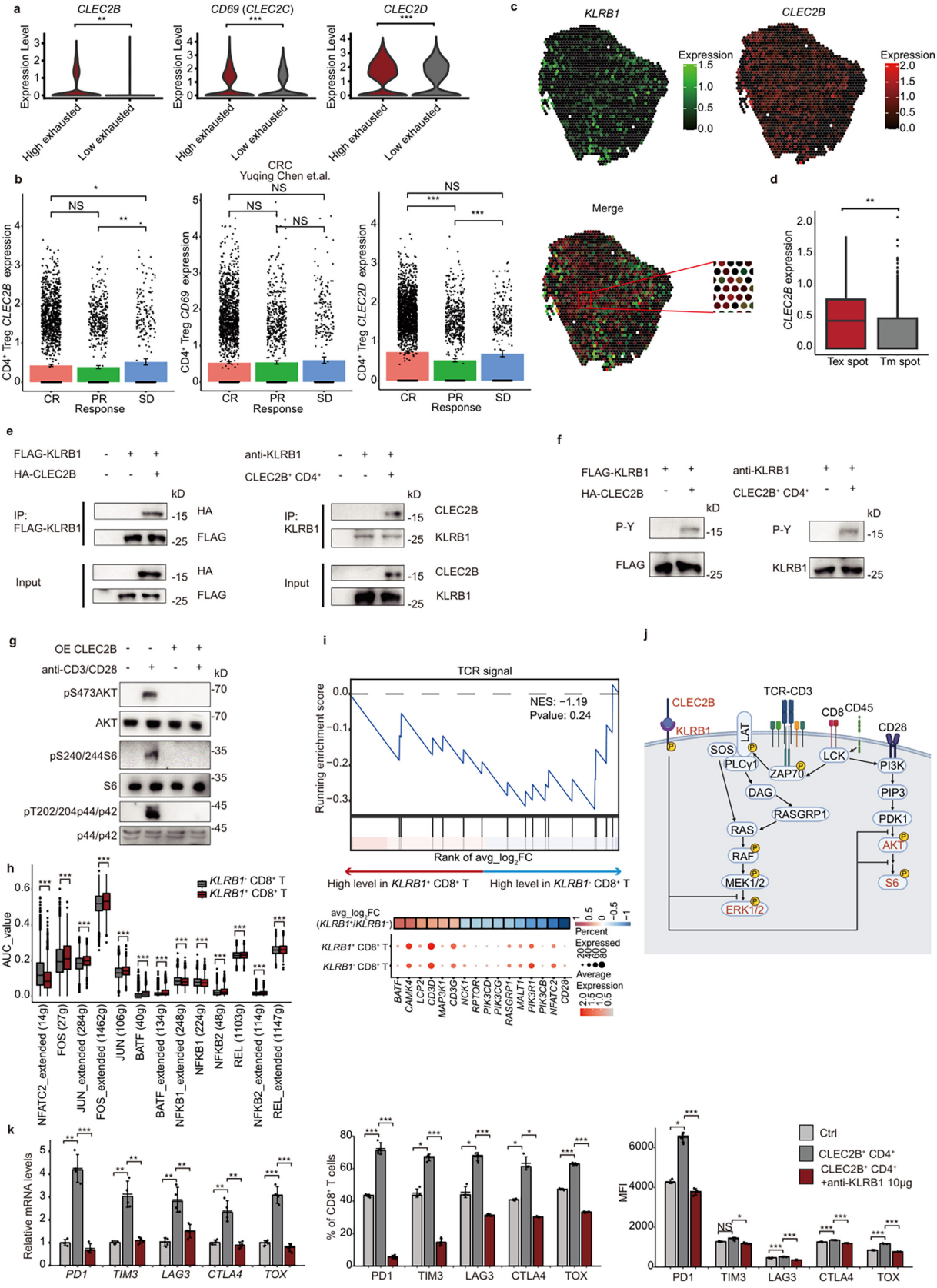

Figure 5 Mechanism of KLRB1 induced exhaustion. (a) KLRB1's ligands expression of CD4+ Tn-like Treg in high and low exhausted groups in scRNA-seq data generated in house. Statistical significance was assessed using two-sided unpaired Student's t-test with heteroscedasticity. **p<0.01, ***p<0.001. (b) KLRB1's ligands expression of CD4+ Treg in different ICB response groups. scRNA-seq dataset are from Chen *et al*.[80] One point represents a cell and bar represents mean expression. Statistical significance was assessed using two-sided unpaired Student's t-test with heteroscedasticity. NS p≥0.05, *p<0.05,

Figure 5 (Continued)

**p<0.01, ***p<0.001. (c) Co-localization visualization of *KLRB1* and *CLEC2B* in spatial transcriptome data of S6_Rep2 sample.[67] (d) *CLEC2B* expression in exhausted CD8+ T cells density high spot and memory CD8+ T cells density high spot in spatial transcriptome data of S6_Rep2 sample.[67] Statistical significance was assessed using a two-sided unpaired Student's t-test with heteroscedasticity. **p<0.01. (e) left panel, western blot analysis showing IP assay performed with purified FLAG-KLRB1 and HA-CLEC2B proteins. HEK293 cells were transfected with FLAG-KLRB1 or/and HA-CLEC2B proteins and cell lysates were incubated with anti-FLAG beads. Then proteins enriched by FLAG beads were tested by western blot. Right panel, western blot analysis showing IP assay performed with endogenous proteins from exhausted CD8+ T cells and CLEC2B+ CD4+ T cells. Human naive CD8+ T cells enriched from PBMC were stimulated with anti-CD3/CD28 antibodies for four times to induce exhaustion. CLEC2B+ CD4+ T cells were sorted from tumors of MSS CRC. Then lysates of sorted cells and lysates of exhausted CD8+ T cells were incubated at 4°C and then immunoprecipitated with anti-KLRB1 antibody (BioLegend 108759, 1:200). Proteins enriched were analyzed by western blot. (f) Left panel, western blot analysis showing phosphorylation of tyrosine of exogenous KLRB1 protein. HEK293 cells were overexpressed with FLAG-KLRB1 and/or HA-CLEC2B proteins. FLAG-KLRB1 protein was enriched by anti-FLAG beads and analyzed by western blot. Tyrosine phosphorylation was immunoblotted with anti-P-Y antibody (Cell Signaling, 8954S, 1:1000). Right panel, western blot analysis showing phosphorylation of tyrosine of endogenous KLRB1 protein. Human naive CD8+ T cells enriched from PBMC were stimulated with anti-CD3/CD28 antibodies for four times to induce exhaustion. CLEC2B+ CD4+ T cells were sorted from tumors of MSS CRC. Then sorted cells and CD8+ T cells were co-cultured and lysed. KLRB1 was IPed with anti-KLRB1 antibody and analyzed by western blot. Tyrosine phosphorylation was immunoblotted with anti-P-Y antibody. (g) Western blot analysis showing phosphorylation of TCR signaling, PI3K-AKT pathway and ERK pathway in CD8+ T cells. Mouse naive CD8+ T cells enriched from spleen were stimulated with anti-CD3/CD28 antibodies for four times to induce exhaustion. HEK293 cells (2×10^6 cells) overexpressed with CLEC2B or control vector were co-cultured with CD8+ T cells (5×10^6 cells). Then cells were treated with anti-CD3/CD28 antibodies for 30 min or not and CD8+ T cells were collected for western blot analysis. (h) TF activity analysis in scRNA-seq data generated in house. Statistical significance was assessed using a two-sided unpaired Student's t-test with heteroscedasticity. ***p<0.001. (i) TCR signaling analysis in scRNA-seq data generated in house. Top, GSEA analysis of TCR signaling. NES <0 indicated that this pathway was less expressed in *KLRB1*+ CD8+ T cells. Bottom, dot plot of differentially expressed genes in TCR signaling and heatmap of avg_log_2FC of corresponding gene. Genes with adjusted p value<0.05 and absolute value of avg_log_2FC more than 0.25 were considered as differentially expressed genes. Only classic CD8+ T cells were included. (j) Schema diagram of KLRB1 suppressive signaling in CD8+ T cells. Figure was created in BioRender. (k) Human exhausted CD8+ T cells (1×10^6 cells) stimulated by anti-CD3/CD28 antibodies for four times were co-cultured with human CLEC2B+ CD4+ T cells sorted from colon cancer of human patients by FACS (1×10^6 cells) and treated with 10 µg anti-KLRB1 antibody or IgG as control. Then CD8+ T cells were enriched by beads and analyzed. The mRNA levels (left panel) and protein levels (middle and right panel) were determined by RT-qPCR and FACS analysis (n=4 per group). Bars represent the median values, data are the mean±SD. NS p≥0.05, *p<0.05, **p<0.01, ***p<0.001 by two-sided unpaired Student's t-test with heteroscedasticity. For the proportion of TIM3-positive cells, the control group data were not normally distributed; for the proportion of LAG-3-positive cells, the control group data were not normally distributed; for the proportion of CTLA4-positive cells, the CD4+ T co-culture group data were not normally distributed; for PD-1 MFI, the control group data were not normally distributed; and for TIM3 MFI, the CD4+ T co-culture group data were not normally distributed. The Wilcoxon test was therefore used in all these cases. AUC, area under the curve; CR, complete response; CRC, colorectal cancer; CTLA4, cytotoxic T-lymphocyte associated protein 4; FACS, fluorescence activated cell sorter; FC, fold change; GSEA, Gene Set Enrichment Analysis; ICB, immune checkpoint blockade; IP, immunoprecipitation; LAG3, lymphocyte activation gene 3; MFI, mean fluorescence intensity; MSS, microsatellite stable; mRNA, messenger RNA; NES, normalized enrichment score; NS, not significant; PBMC, peripheral blood mononuclear cell; PD-1, programmed cell death protein 1; PR, partitial response; RT-qPCR, real-time quantitative reverse transcription polymerase chain reaction; scRNA-seq, single-cell RNA sequencing; TCR, T-cell receptor; TF, transcription factor; TIM3, T-cell immunoglobulin and mucin-domain containing molecule 3; TOX, thymocyte selection-associated high mobility group box; Tex, exhausted T cell; Tm, memory T cell; Tn-like Tex, naïve-like exhausted T cell; Treg, regulatory T cell; SD, stable disease.

The binding of the inhibitory receptor with the ligand stimulates inhibitory signals in CD8+ T cells.[42] Therefore, spatial proximity between the receptor and ligand is essential for the receptor to exhibit cytoplasmic function in CD8+ T cells. We profiled the spatial transcriptome of MSS CRC at single-cell resolution and combined it with scRNA-seq analysis. Co-occurrence, cell communication, and ligand-receptor co-localization analysis uncovered the interaction of the ligand-receptor pair, *CLEC2B-KLRB1*. Indeed, the interaction of CLEC2B-KLRB1 elicits transduction of suppressive signaling to induce exhaustion, while blockade of their ligation by KLRB1 antibody effectively inhibits the exhaustion program in CD8+ T cells. Therefore, our study identified CLEC2B-KLRB1 as a new immune checkpoint for CD8+ T cells and a promising target for immunotherapy.

KLRB1 is a protein encoded in the NK gene complex. Therefore, KLRB1 is initially thought to be one marker for NK cells. However, the expression of KLRB1 was then documented in other cell types, including CD4+ T cells and CD8+ T cells[43 44], γδT cells,[45] mucosal-associated invariant T cell (MAIT) cells,[46] and myeloid cells.[47] While analyzing scRNA-seq data of ICB poor responsive patients, we found *KLRB1* is highly expressed on CD8+ T cells, which account for a large proportion of not only MSS CRC, but also other cancers. These results raised the question of whether KLRB1 regulates CD8+ T cells. In view of its inhibitory function in NK cells,[48 49] an inhibitory function of TCR signaling was hypothesized. Detailed expression analysis revealed that KLRB1 is highly expressed in terminally exhausted CD8+ T cells. Functional studies further demonstrated that KLRB1 is an exhaustion-promoting gene. Ligand binding

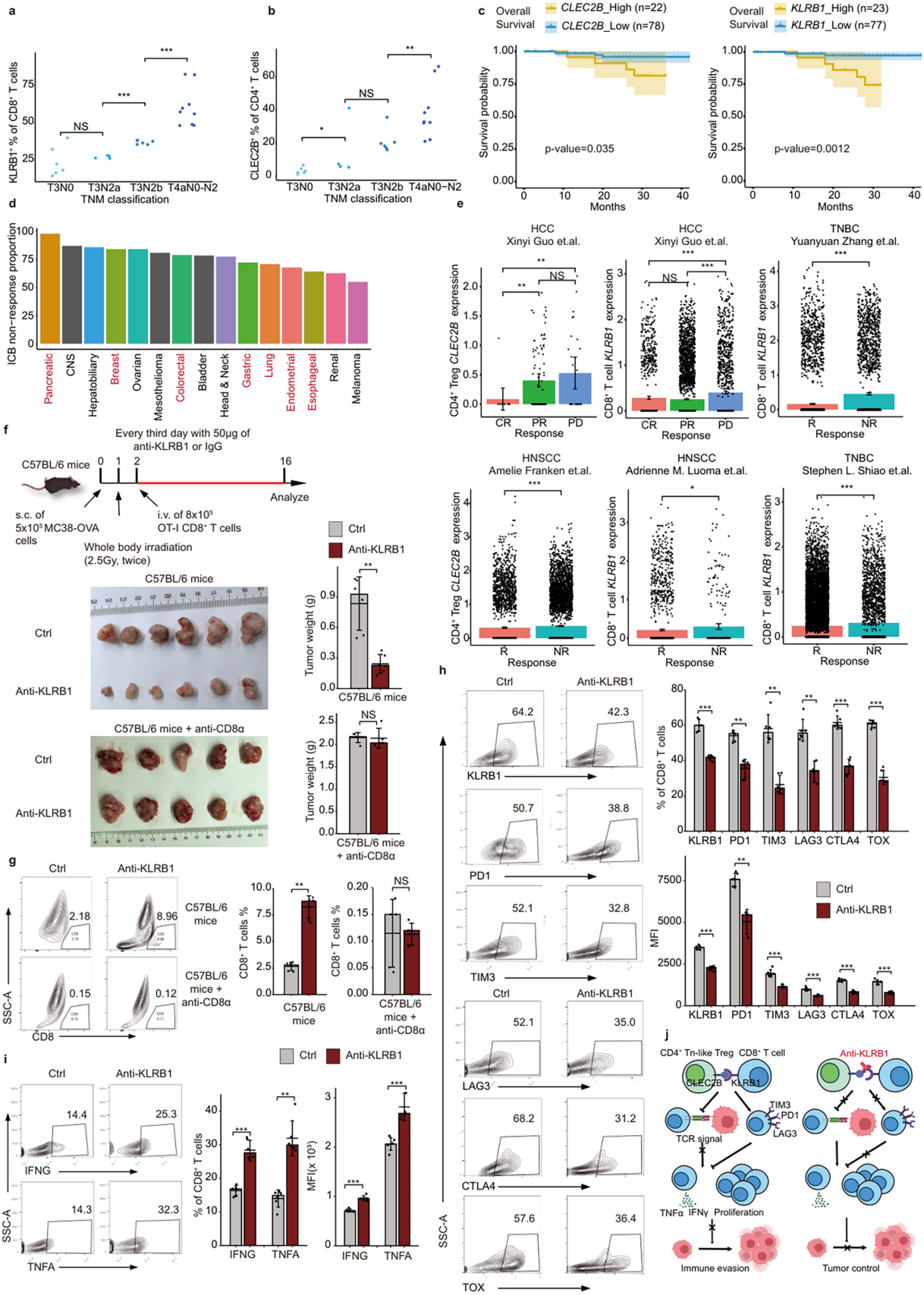

Figure 6 KLRB1 as an immune checkpoint receptor to target. (a–b) Each dot represents a patient with CRC MSS sample. (a) The association of proportion of KLRB1$^+$ cells in CD8$^+$ T cells with tumor progression stages. (b) The association of proportion of CLEC2B$^+$ cells in CD4$^+$ T cells with tumor progression stages. Tumors of MSS CRC were collected and digested

Figure 6 (Continued)

into single cells and analyzed by FACS analysis. Statistical significance was assessed using two-sided unpaired Student's t-test with heteroscedasticity. For the proportion of KLRB1-positive cells, the data for the T4aN0–N2 group were not normally distributed; for the proportion of CLEC2B-positive cells, the data for the T3N2a and T3N2b groups were not normally distributed. The Wilcoxon test was therefore used in these cases. NS p≥0.05, *p<0.05, **p<0.01, ***p<0.001. (c) Survival analysis of CLEC2B and KLRB1 expression in patients with colon adenocarcinoma. Bulk RNA-seq data were from cBioPortal for Cancer Genomics.[87] The shaded area represents the 95% CI. Statistical significance was assessed using the log-rank test. (d) ICB non-response proportion of pan-cancer. ICB-response information of pan-cancer was from Chang *et al*.[79] Cancer types with high proportion of KLRB1$^+$ CD8$^+$ T cells in figure 3c and positive correlation between KLRB1 and exhaustion score in figure 3e are highlighted in red. (e) CLEC2B expression in CD4$^+$ Treg and KLRB1 expression in CD8$^+$ T cells in different ICB response groups. scRNA-seq datasets are from Franken *et al*,[81] Guo *et al*,[82] Zhang *et al*,[83] Luoma *et al*[84] and Shiao *et al*.[85] One point represents a cell and the bar represents mean expression. Only classic CD8$^+$ T cells are included. Statistical significance was assessed using a two-sided unpaired Student's t-test with heteroscedasticity. *p<0.05, **p<0.01, ***p<0.001. (f–i) n=6 or 5 (anti-CD8α) per group f, upper panel, C57BL/6 mice injected subcutaneously with 5×10^5 MC38-OVA cells were immunodepleted by irradiation (2.5 Gy, two times). Naive OT-I CD8$^+$ T cells were stimulated with OVA$_{257–264}$ peptide for 24 hours and adoptively transferred by tail vein injection (i.v.) 1 day post irradiation. For the following 14 days (red line), mice were intraperitoneal injected with 50 µg anti-KLRB1 antibody (mouse IgG2a κ, BioLegend 108759, clone PK136) or IgG (mouse IgG2a κ isotype control antibody, BioLegend 401502, clone MG2a-53) as control every third day. To deplete endogenous CD8$^+$ T cells, C57BL/6 mice were intraperitoneally injected with anti-CD8α (100 µg of anti-CD8 antibody (clone YTS169.4), two times). Then mice were injected subcutaneously with 5×10^5 MC38-OVA cells and intraperitoneal injected with 50 µg anti-KLRB1 antibody or IgG as control every third day. Tumor burden was measured (f) bottom panel. Tumor-infiltrated CD8$^+$ T cells (g), percentage and MFI of KLRB1 and exhaustion proteins (h), cytokines and KI67 (i) were measured by FACS analysis. Bars represent the median values, data are the mean±SD. NS p≥0.05, *p<0.05, ***p<0.001 by two-sided unpaired Student's t-test with heteroscedasticity. For tumor weight, the CD8$^+$ T-cell depletion plus KLRB1 antibody group data were not normally distributed; for the proportion of CD8$^+$ T cells, the KLRB1 antibody group data were not normally distributed; for the proportion of PD-1-positive cells, the KLRB1 antibody group data were not normally distributed; for the proportion of TIM3-positive cells, the control group data were not normally distributed; for the proportion of LAG-3-positive cells, the control group data were not normally distributed; for PD-1 MFI, the KLRB1 antibody group data were not normally distributed; and for the proportion of TNF-α-positive cells, the KLRB1 antibody group data were not normally distributed. The Wilcoxon test was therefore used in all these cases. (f) Was created in BioRender. (j) Summary diagram of CLEC2B-KLRB1 as an immune checkpoint. Figure was created in BioRender. CNS, central nervous system; CRC, colorectal cancer; CTLA4, cytotoxic T-lymphocyte associated protein 4; FACS, fluorescence activated cell sorter; HCC, hepatocellular carcinoma; HNSCC, head and neck squamous cell carcinoma; ICB, immune checkpoint blockade; IFN, interferon; i.v., intravenous; LGA-3, lymphocyte activation gene 3; MFI, mean fluorescence intensity; MSS, microsatellite stable; mRNA, messenger RNA; NR, non-response; NS, not significant; PD-1, programmed cell death protein 1; R, response; RNA-seq, RNA sequencing; scRNA-seq, single-cell RNA sequencing; s.c., subcutaneous injections; TCR, T-cell receptor; TIM3, T-cell immunoglobulin and mucin-domain containing molecule 3; TNBC, triple-negative breast cancer; TNF, tumor necrosis factor; TNM, tumor, node, metastases; TOX, thymocyte selection-associated high mobility group box; Treg, regulatory T cell.

on KLRB1 drives phosphorylation of tyrosine and induces transduction of inhibitory signals in CD8$^+$ T cells. Together, our work discovered KLRB1, a classic NK marker, acts as an immune checkpoint receptor in CD8$^+$ T cells.

The role of KLRB1 in cancer remains controversial and appears to be context-dependent. For instance, in breast cancer,[50–52] endometrial cancer,[53] lung adenocarcinoma,[54 55] and HCC,[56 57] most studies indicate that high KLRB1 expression is associated with favorable prognosis and enhanced immune cell infiltration. However, a notable exception in HCC research[58] suggests that a specific subset of CD8$^+$ T cells with high KLRB1 expression, distinct from exhausted T cells, exhibits low cytotoxicity and proliferation and is linked to poor prognosis in early recurrent cases. These conflicting findings underscore that the function of KLRB1 requires further in-depth investigation. Since the specific role of KLRB1 in CRC had not been previously elucidated, our study reveals its immunosuppressive function within CD8$^+$ T cells in the CRC microenvironment.

METHODS

Clinical sample collection and preparation

All enrolled patients were preoperatively histopathologically confirmed with colorectal adenocarcinoma. Patients with autoimmune diseases, prior malignancies, or history of preoperative chemotherapy, radiotherapy, or immunotherapy were excluded. Tumor tissues were collected within 15 min of surgical excision following thorough clearance of blood and necrotic tissue. Comprehensive pathological profiles of the patients were detailed in online supplemental table 1. All specimen collections were performed at Peking University Shougang Hospital.

Animals

6–8 weeks old C57BL/6 mice were purchased from Vital River Laboratory Animal Technology and used for and CD8$^+$ T-cell isolation. 6–8 weeks old OT-I mice were purchased from The Jackson Laboratory and used for OT-I CD8$^+$ T-cell isolation. All of the mice were maintained in pathogen-free facilities and used strictly in accordance with the protocols approved by the IACUC of Tsinghua University. The study is compliant with all of the relevant ethical regulations regarding animal research. Sex was not considered in the study design and analysis since this study was not designed to detect sex differences. Only male mice were used for this study, and all mouse data were collected from male mice.

Cell lines

The MC38-OVA cell and B16-OVA cells were from P Jiang laboratory (Tsinghua University, Beijing). 293T cells were purchased from the American Type Culture Collection (CRL-3216). MC38-OVA cells, B16-OVA cells, and 293T cells were cultured in Dulbecco's Modified Eagle Medium (DMEM) medium (macgene, CM10013). Primary $CD4^+$ and $CD8^+$ T cells were cultured in Roswell Park Memorial Institute (RPMI)-1640 medium (macgene, CM10041). All cell lines have been authenticated and were tested for *Mycoplasma* contamination. No such commonly misidentified cell lines were used in this work. Furthermore, we have authenticated all the cell lines by using the short tandem repeat profiling method according to the reported protocol.

Single-Cell RNA sequencing

Cell capture and cDNA synthesis

Cell isolation and complementary DNA (cDNA) preparation were performed using the Single Cell 3' Library and Gel Bead Kit V3.1 (10x Genomics, 1000121) and the Chromium Single Cell G chip (10x Genomics, 1000120). The cell suspension, with a concentration of 300–600 viable cells per microliter (determined via Count Star), was loaded onto the Chromium Single Cell Controller (10x Genomics) to encapsulate individual cells into gel beads within an emulsion, following the manufacturer's instructions. Briefly, cells were resuspended in phosphate-buffered saline (PBS) supplemented with 0.04% Bovine Serum Albumin (BSA). Approximately 10,000 cells were introduced into each channel, with an estimated recovery of 9,000–10,000 cells. Encapsulated cells were lysed, and their RNA was subjected to barcoding during reverse transcription within individual gel beads. Reverse transcription was carried out on an S1000 Touch Thermal Cycler (Bio-Rad) at 53°C for 45 min, followed by a 5-minute incubation at 85°C, and then held at 4°C. The resulting cDNA was amplified, and its quality was assessed using an Agilent 4200 platform (CapitalBio Technology, Beijing).

Single cell RNA-Seq library preparation

scRNA-seq libraries were prepared following the manufacturer's protocol (10x Genomics) using the Single Cell 3′ Library and Gel Bead Kit V3.1. The final libraries underwent paired-end sequencing (150 bp read length, PE150) on an Illumina NovaSeq 6000 platform, with a minimum sequencing depth of 100,000 reads per cell. All sequencing procedures were conducted by CapitalBio Technology (Beijing).

scRNA-seq data processing and quality control

The raw fastq data were inputted to Cell Ranger V.7.0.1 (10x Genomics Cell Ranger V.7.0.1) to get read counts with GRCh38 as the reference genome. Three output files of the function "cellranger count" were sent to Seurat V.5.2.1[59] for downstream analysis. Cells were filtered if mitochondria genes Unique Molecular Identifier (UMI) percentage was more than 25% or gene numbers were more than 7,000 or less than 200. Doublets were removed as described in the annotation sections.

Clustering and major cell type annotation

We used Seurat V.5.2.1[59] default workflow to process the count matrix. The count matrix was normalized by the function "NormalizeData" to remove the difference of total UMI counts. 2,000 variable genes were found by the function "FindVariableFeatures" and all genes were scaled across cells by the function "ScaleData". With no obvious batch effect, samples were integrated simply by merging. Principal component analysis was performed on the scaled data to reduce the dimensionality and capture the main sources of variation in the dataset. Then the top 50 Principal Components (PCs) were chosen to identify clusters by the shared nearest neighbor algorithm. Finally, the function "RunUMAP" was used to visualize the clustering result in two dimensions.

Then, we annotated the clusters according to known marker genes: epithelial cell ($EPCAM^+$, $CDH1^+$),[60 61] stromal cell ($PECAM1^+$, $CDH5^+$, VWF^+, DCN^+, $COL3A1^+$, $SYNPO2^+$, $RGS5^+$),[60–62] T cell/NK cell ($PTPRC^+$, $CD3D^+$, $CD3E^+$, $CD3G^+$, $KLRD1^+$),[60] B cell ($PTPRC^+$, $CD79A^+$, $MS4A1^+$),[60 61] myeloid cell ($CD68^+$, $CD14^+$, $CSF3R^+$, $FCGR3B^+$),[60–63] TN doublet (T cell/neutrophil doublet) which showed high expression of T cell and neutrophil markers, and Epi-immune doublet (epithelial cell/immune cell doublet) which showed high expression of epithelial cell and immune cell markers. Two clusters of doublet were not included in the downstream analysis.

Clustering and subset cell type annotation

Epithelial cell

Epithelial cell was extracted from total cells using the function "subset". To avoid the influence of patient heterogeneity on clustering, we used the harmony algorithm to integrate cells from different patients. Then the same data processing and clustering analysis as total cells were performed. To distinguish malignant cells from normal cells, we employed copy number variation (CNV) scores. Infercnv V.1.14.2 (https://github.com/broadinstitute/inferCNV) was used to calculate CNV of each gene from chromosome 1 to chromosome 22 with stromal cells as normal control.

CNV score was calculated as follows:

$$\sum_{i=1}^{n} \left(CNV_i - 1\right)^2 \text{CNV score}$$

We annotated the clusters according to CNV score, known marker genes and highly expressed genes: goblet cell ($REG4^+$, $MUC2^+$),[60] enterocyte ($SLC26A3^+$, $CA1^+$, $GUCA2A^+$)[60], normal, malignant, Epi-immune doublet (epithelial cell/immune cell doublet) which showed high expression of epithelial cell and immune cell markers, and Epi-Mast doublet (epithelial cell/mast cell doublet) which showed high expression of epithelial cell and mast cell markers. Two clusters of doublet were not included in the downstream analysis.

Stromal cell

Stromal cell was extracted from total cells using function "subset". Then the same data processing and clustering analysis as total cells was performed. We annotated

the clusters according to known marker genes and highly expressed genes: vascular SMC (vascular smooth muscle cell; *SYNPO2*$^+$, *CNN1*$^+$)[60], pericyte (*CSPG4*$^+$, *ABCC9*$^+$, *KCNJ8*$^+$),[60] prolif Stro (proliferating stromal cell; *MKI67*$^+$, *UBE2C*$^+$), *SFRP2*$^+$ Fibro (*SFRP2*$^+$ fibroblast; *DCN*$^+$, *COL3A1*$^+$, *SFRP2*$^+$)[62], *AGT*$^+$ Fibro (*AGT*$^+$ fibroblast; *DCN*$^+$, *COL3A1*$^+$, *AGT*$^+$),[62] *CCL13*$^+$ Fibro (*CCL13*$^+$ fibroblast; *DCN*$^+$, *COL3A1*$^+$, *CCL13*$^+$)[62], *NRG1*$^+$ Fibro (*NRG1*$^+$ fibroblast; *DCN*$^+$, *COL3A1*$^+$, *NRG1*$^+$),[62] *TEX14*$^+$ Fibro (*TEX14*$^+$ fibroblast; *DCN*$^+$, *COL3A1*$^+$, *TEX14*$^+$),[62] LEC (lymphatic endothelial cell; *PECAM1*$^+$, *CDH5*$^+$, *LYVE1*$^+$, *PROX1*$^+$),[60 61] *HECW2*$^+$ Endo (*HECW2*$^+$ endothelial cell; *PECAM1*$^+$, *CDH5*$^+$, *HECW2*$^+$),[61] *ACKR1*$^+$ Endo (*ACKR1*$^+$ endothelial cell; *PECAM1*$^+$, *CDH5*$^+$, *ACKR1*$^+$),[61] *GJA5*$^+$ Endo (*GJA5*$^+$ endothelial cell; *PECAM1*$^+$, *CDH5*$^+$, *GJA5*$^+$),[61] Stro-Epi doublet (stromal cell/epithelial cell doublet) which showed high expression of stromal cell and epithelial cell markers, Stro-immune doublet (stromal cell/immune cell doublet) which showed high expression of stromal cell and immune cell markers, and Stro-B doublet (stromal cell/B-cell doublet) which showed high expression of stromal cell and B-cell markers. Three clusters of doublet were not included in the downstream analysis.

B cell

B cell was extracted from total cells using function "subset". Then the same data processing and clustering analysis as total cells was performed. We annotated the clusters according to known marker genes and highly expressed genes: Bn (naïve B cell; *IGHD*$^+$, *SELL*$^+$, *FCER2*$^+$),[64] Bfoc (follicular B cell; *RGS13*$^+$, *LMO2*$^+$)[64], Bgc (Germinal center B cell; *CD69*$^+$, *NR4A2*$^+$, *CXCR4*$^+$)[64], Bp IgA (IgA generating plasma B cell; *SDC1*$^+$, *MZB1*$^+$, *XBP1*$^+$, *IGHA1*$^+$, *IGHA2*$^+$),[64] Bp IgG (IgG generating plasma B cell; *SDC1*$^+$, *MZB1*$^+$, *XBP1*$^+$, *IGHG1*$^+$, *IGHG2*$^+$),[64] Bp Prolif (proliferating plasma B cell; *SDC1*$^+$, *MZB1*$^+$, *XBP1*$^+$, *MKI67*$^+$, *UBE2C*$^+$),[64] B-Epi doublet (B cell/epithelial cell doublet) which showed high expression of B cell and epithelial cell markers, B-T doublet (B cell/T-cell doublet) which showed high expression of B cell and T-cell markers, and B-Neu doublet (B cell/neutrophil doublet) which showed high expression of B cell and neutrophil markers. Three clusters of doublet were not included in the downstream analysis.

T cell/NK cell

T cell/NK cell was extracted from total cells using function "subset". Then the same data processing and clustering analysis as total cells was performed. We annotated the clusters according to known marker genes and highly expressed genes: CD8$^+$ Tem (CD8$^+$ effector memory T cell; *CD8A*$^+$, *CD8B*$^+$, *GZMK*$^+$),[16] CD8$^+$ Trm (CD8$^+$ resident memory T cell; *CD8A*$^+$, *CD8B*$^+$, *XCL1*$^+$, *XCL2*$^+$, *MYADM*$^+$),[16] CD8$^+$ Tn-like Tex (CD8$^+$ naïve-like exhausted T cell; *CD8A*$^+$, *CD8B*$^+$, *LEF1*$^+$, *TCF7*$^+$, *CD27*$^+$, *HAVCR2*$^+$, *TOX*$^+$),[16] CD8$^+$ Tex (CD8$^+$ exhausted T cell; *CD8A*$^+$, *CD8B*$^+$, *HAVCR2*$^+$, *TOX*$^+$),[16] CD8$^+$ MAIT (CD8$^+$ mucosal-associated invariant T cell; *CD8A*$^+$, *CD8B*$^+$, *SLC4A10*$^+$),[16] CD8$^+$ IEL (CD8$^+$ intraepithelial lymphocyte; *CD8A*$^+$, *CD8B*$^+$, *CD160*$^+$, *KIR2DL4*$^+$),[16] CD4$^+$ Tn (CD4$^+$ naïve T cell; *CD4*$^+$, *LEF1*$^+$, *TCF7*$^+$),[16] CD4$^+$ Tcm (CD4$^+$ central memory T cell; *CD4*$^+$, *CCR7*$^+$, *ANXA1*$^+$),[16] CD4$^+$ Treg (CD4$^+$ regulatory T cell; *CD4*$^+$, *FOXP3*$^+$, *IL2RA*$^+$),[16] CD4$^+$ Tn-like Treg (CD4$^+$ naïve-like regulatory T cell; *CD4*$^+$, *FOXP3*$^+$, *IL2RA*$^+$, *SELL*$^+$),[16] CD4$^+$ Tprolif (CD4$^+$ proliferating T cell; *CD4*$^+$, *MKI67*$^+$, *UBE2C*$^+$), CD4$^+$ MAIT (CD4$^+$ mucosal-associated invariant T cell; *CD4*$^+$, *SLC4A10*$^+$),[16] CD4$^+$ IEL (CD4$^+$ intraepithelial lymphocyte; *CD4*$^+$, *CD160*$^+$),[16] CD4$^+$ *PDCD1*$^+$ T (*CD4*$^+$, *PDCD1*$^+$), CD4$^+$ *DAPK2*$^+$ T (*CD4*$^+$, *DAPK2*$^+$), *SLC35F1*$^+$ T (*SLC35F1*$^+$), Trm (resident memory T cell; *CD69*$^+$),[16] *FGFBP2*$^+$ NKT (*FGFBP2*$^+$ natural killer T cell; *CD3D*$^+$, *CD3E*$^+$, *CD3G*$^+$, *KLRF1*$^+$, *FGFBP2*$^+$),[60] IEL-like NKT (intraepithelial lymphocyte-like natural killer T cell; *CD3D*$^+$, *CD3E*$^+$, *CD3G*$^+$, *KLRF1*$^+$, *CD160*$^+$, *KIR2DL4*$^+$),[16 60] ILC3 (type 3 innate lymphoid cell; *KRT86*$^+$, *LST1*$^+$),[64] and unknown cluster which was not included in the downstream analysis.

Myeloid cell

Myeloid cell was extracted from total cells using function "subset". Cells with *IGHG3*, *IGHGP*, *IGLC3*, *IGHG1*, *IGHG4* and *IGHA2* normalized expression more than one were removed. Then the same data processing and clustering analysis as total cells was performed. We annotated the clusters according to known marker genes and highly expressed genes: *CTSG*$^+$ Mast (*CTSG*$^+$ mast cell; *KIT*$^+$, *CPA3*$^+$, *CTSG*$^+$),[16 60] *PRDM16*$^+$ Mast (*PRDM16*$^+$ mast cell; *KIT*$^+$, *PRDM16*$^+$),[16 60] *ATP10D*$^+$ Mast (*ATP10D*$^+$ mast cell; *CPA3*$^+$, *ATP10D*$^+$),[16 60] *S100A8*$^+$ Neu (*S100A8*$^+$ neutrophil; *CSF3R*$^+$, *FCGR3B*$^+$, *S100A8*$^+$),[61] *CCL3L1*$^+$ Neu (*CCL3L1*$^+$ neutrophil; *CSF3R*$^+$, *FCGR3B*$^+$, *CCL3L1*$^+$),[61] *IFIT3*$^+$ Neu (*IFIT3*$^+$ neutrophil; *CSF3R*$^+$, *FCGR3B*$^+$, *IFIT3*$^+$),[61] cDC1 (classic dendritic cell type 1; *XCR1*$^+$, *CLEC9A*$^+$),[61] cDC2 (classic dendritic cell type 2; *FCER1A*$^+$, *CD1C*$^+$),[61] *CCL19*$^+$ mDC (myeloid dendritic cell; *CCL19*$^+$, *LAMP3*$^+$, *CCR7*$^+$),[64] *THBS1*$^+$ Mono (*THBS1*$^+$ monocyte; *FCN1*$^+$, *S100A12*$^+$, *THBS1*$^+$),[62 64] *MARCO*$^+$ Mono (*MARCO*$^+$ monocyte; *FCN1*$^+$, *S100A12*$^+$, *MARCO*$^+$)[62 64], *IL23A*$^+$ Mac (*IL23A*$^+$ macrophage; *MSR1*$^+$, *MRC1*$^+$, *IL23A*$^+$),[62 64] proliferating Mac (proliferating macrophage; *MSR1*$^+$, *MRC1*$^+$, *MKI67*$^+$),[64 65] *C1QC*$^+$ Mac (*C1QC*$^+$ macrophage; *MSR1*$^+$, *MRC1*$^+$, *C1QC*$^+$, *C1QA*$^+$, *APOE*$^+$),[62 64] Mast-T doublet (mast cell/T-cell doublet) which showed high expression of mast cell and T-cell markers, and pDC-Epi doublet (plasmacytoid dendritic cell/epithelial cell doublet) which showed high expression of plasmacytoid dendritic cell[16] and epithelial cell markers. Two clusters of doublet were not included in the downstream analysis.

Classic CD8$^+$ T-cell differential trajectory analysis

Classic CD8$^+$ T cells included CD8$^+$ Tem, CD8$^+$ Trm, CD8$^+$ Tn-like Tex and CD8$^+$ Tex. Monocle V.2.26.0[66] toolkit was used to analyze differential trajectory of Classic CD8$^+$ T cell. Count matrix was inputted to create CellDataSet object. Then function "estimateSizeFactors" was employed to estimate library size and dispersion.

Differentially expressed genes among four subsets were detected by function "differentialGeneTest". Top 1,000 genes detected in more than 5% of cells with q value<0.05 were chosen to establish trajectory using DDRTree algorithm. Finally, the start point of pseudotime was defined in branch which had high proportion of $CD8^+$ Tem.

$CD8^+$ T-cell choosing

All $CD8^+$ T cells ($CD8^+$ Tem, $CD8^+$ Trm, $CD8^+$ Tn-like Tex, $CD8^+$ Tex, $CD8^+$ MAIT and $CD8^+$ IEL) were included in $CD8^+$ T-cell infiltration and $CD8^+$ Tex proportion calculating. In all analyses involving KLRB1, only classic $CD8^+$ T cells were selected and non-classic $CD8^+$ T cells (MAIT, IEL, NKT and γδT) were excluded.

Spatial transcriptome data collection and MSI status prediction

Spatial transcriptome data were collected from public literatures,[63 67–69] only treatment-naïve samples were included. MAP V.0.1.0[70] was used to predict MSI status. The raw UMI count matrix was normalized via total UMI count scaling, and then the gene expressions of all cells were summed to generate pseudobulk data. After applying $\log_2(x+1)$ transformation, the "runMAP" function was used to predict the MSI status.

Spatial transcriptome data annotation

cell2location V.0.1.3[17] was used to annotate spatial transcriptome data at the subset level. $CD8^+$ Tn-like Tex and $CD8^+$ Tex were combined as "$CD8^+$ Tex"; $CD4^+$ *PDCD1*$^+$ T, $CD4^+$ *DAPK2*$^+$ T, *SLC35F1*$^+$ T and Trm were not included in annotation. Then we followed the default workflow of cell2location: mitochondrial genes removal, choosing our scRNA-seq data as reference, gene filtering with default parameters (cell_count_cut-off=5, cell_percentage_cut-off2=0.03, non-z_mean_cut-off=1.12), estimation of reference cell type signatures with patient as batch_key and training with 1,000 epochs, creating an annotation model using two parameters (N_cells_per_location=5 and detection_alpha=20) and training with 10,000 epochs. Finally, we used the 5% quantile of the posterior distribution as recommended in tutorials, representing the value of cell abundance (or called cell density).

Signature score analysis

The signature gene set of each subset type was composed of the top 30 genes with the highest avg_$\log_2$ fold change (FC) (adjusted p value<0.05) and known marker genes (online supplemental table 3). There was no overlap between any two signature gene lists. Exhaustion score was calculated using the signature gene set of $CD8^+$ Tex. Function "AddModuleScore" was used to get the signature score.

Cell–cell co-localization analysis

Every spot had a density of all subsets deconvoluted by cell2location. Calculate the Spearman correlation in density between all subsets and $CD8^+$ Tex. A positive correlation coefficient means cell–cell co-localization. To further confirm the co-localization result, the Spearman correlation in signature score between selected subsets and $CD8^+$ Tex was calculated, and a positive correlation coefficient means cell co-localization. The Benjamini-Hochberg method was used for multiple testing correction.

Cell enrichment analysis

To detect subsets enriched in the high exhausted group, we used χ^2 test. For subset x, we classified cells into four groups (x from high exhausted group patients, non-x from high exhausted group patients, x from low exhausted group patients, non-x from low exhausted group patients; non-x means other subsets within the lineage) and counted the cell number of each group. χ^2 test was used to test if subset x was enriched in the high exhausted group and Ro/e was calculated as the observed cell number divided by the expected cell number. The macrophage lineage was composed of *IL23A*$^+$ Mac, proliferating Mac and *C1QC*$^+$ Mac. The dendritic cell lineage was composed of cDC1, cDC2 and *CCL19*$^+$ mDC. The NKT lineage was composed of *FGFBP2*$^+$ NKT and IEL-like NKT. The $CD4^+$ T-cell lineage was composed of $CD4^+$ Tn, $CD4^+$ Tcm, $CD4^+$ Treg, $CD4^+$ Tn-like Treg, $CD4^+$ Tprolif, $CD4^+$ MAIT, $CD4^+$ IEL, $CD4^+$ *PDCD1*$^+$ T and $CD4^+$ *DAPK2*$^+$ T.

Cell–cell communication

Cell–cell communication networks between $CD8^+$ Tex cells and four $CD8^+$ Tex-associated subsets were systematically interrogated using CellChat V.2.1.2[23] following standard analytical pipelines. The whole scRNA-seq data generated in-house was converted into a CellChat object via the function "createCellChat". Set all interactions in CellChatDB.human as the reference database. Then identify highly expressed genes and interactions by using function "identifyOverExpressedGenes" and "identifyOverExpressedInteractions" separately. Permutation test-based significance testing of interactions was completed in function "computeCommunProb" with parameter "type" set as "triMean". To ensure analytical reliability, low-confidence interactions involving cell populations with <10 cells in either sender or receiver compartments were excluded using function "filterCommunication". Finally, we summarized communication number and weight at the pathway and subset level by using function "computeCommunProbPathway" and "aggregateNet".

Ligand-receptor co-localization analysis

We performed a Spearman correlation analysis of ligand and receptor expression in spatial transcriptome data, where higher correlation coefficients indicate higher co-localization levels. To further validate the co-localization result, we first computed the expression products at each spatial spot. By performing 1,000 permutations of the spatial distribution of genes, we generated the distribution of mean products at random conditions. Statistical significance was determined using a permutation test.

Differential expression analysis

Classic $CD8^+$ T cells with *KLRB1* normalized expression more than 0 were defined as *KLRB1*$^+$ $CD8^+$ T cells. To identify differentially expressed genes between *KLRB1*$^+$ $CD8^+$ T cells and *KLRB1*$^-$ $CD8^+$ T cells, we used function "FindMarkers" with "test.use" parameter set to "MAST". Genes with adjusted p value <0.05 and absolute value of avg_log_2FC more than 0.25 were considered as differentially expressed genes.

Tex spots versus memory T cell (Tm) spots analysis

Density of subsets were calculated by cell2location as described above. Spatial spots with $CD8^+$ Tex density ranking in the top 30% and memory T cell ($CD8^+$ Trm and $CD8^+$ Tem) density in the bottom 50% were defined as exhausted spots. While spots with memory T cell ($CD8^+$ Trm and $CD8^+$ Tem) density ranking in the top 30% and $CD8^+$ Tex density in the bottom 50% were defined as memory spots.

Gene Set Enrichment Analysis

Genes in the TCR signaling pathway (online supplemental table 4) were collected according to literature,[37 71–73] Cell Signaling Technology pathway "T Cell Receptor Signaling" (https://www.cellsignal.cn/pathways/t-cell-receptor-signaling) and Kyoto Encyclopedia of Genes and Genomes (KEGG) pathway "T cell receptor signaling pathway" (https://www.kegg.jp/pathway/map04660) and "PI3K-Akt signaling pathway" (https://www.kegg.jp/pathway/map04151). clusterProfiler V.4.6.2[74] and GseaVis V.0.1.1 (https://github.com/junjunlab/GseaVis) were used to complete Gene Set Enrichment Analysis (GSEA) and visualization.

TF activity analysis

Standard flow work of SCENIC[75] was used to calculate the activity of TFs. Only classic $CD8^+$ T cells were included.

Survival analysis

Kaplan-Meier survival curve was generated and statistically analyzed using the ggsignif V.0.6.4 (https://github.com/const-ae/ggsignif). Survival differences between groups were assessed through log-rank tests, with p values<0.05 considered statistically significant.

Isolation and stimulation of primary $CD8^+$ T cells

Mouse $CD8^+$ T cells were isolated from mouse spleens using a biotin selection kit. Unless otherwise indicated, mouse $CD8^+$ T cells were stimulated with 3.5 µg/mL anti-CD3 and 1 µg/mL anti-CD28 antibodies. The OT-I $CD8^+$ T cells from OT-I mice were stimulated with 1 µg/mL $OVA_{257–264}$ (SIINFEKL) peptide. All $CD8^+$ T cells were cultured in RPMI-1640 medium (macgene, CM10041) with 100 U/mL interleukin-2. For in vitro exhaustion, $CD8^+$ T cells were stimulated four times with 2 days' interval.

Primary human $CD8^+$ T cells

peripheral blood mononuclear cells (PBMCs) were collected from healthy donors, and mononuclear cells were separated from peripheral blood by Ficoll gradient centrifugation. $CD8^+$ T cells were isolated using magnetic beads. $CD8^+$ T cells were stimulated with 3.5 µg/mL anti-CD3 and 1 µg/mL anti-CD28 antibodies.

Dissociation of tumor-infiltrating cells from primary tissues

Clinical or mouse tumor samples were enzymatically digested into single cells. The clinical samples were cut into small pieces and washed by PBS. Then, samples were added with collagenase IV and shaken at 37°C for 1.5 hours for digestion. The digested samples were filtered through a single-cell strainer to remove tissue debris. After washing, the samples were ready for subsequent flow cytometry analysis. For cytokine analysis, samples were treated with anti-CD3, anti-CD28 antibodies and Brefeldin A/Monensin for 5 hours prior to flow cytometry analysis.

Multiplex immunohistochemistry

A five-color multiplex immunohistochemistry panel (PanCK, C2562, Sigma-Aldrich; CD8A, CST70306, Cell Signaling Technology; TIM3, CST45208, Cell Signaling Technology; KLRB1, ab197979, Abcam Plc) was used for sequential antigen detection. Primary antibodies targeting distinct markers were progressively administered (PanCK, 2,000×, incubation at room temperature (RT) for 30 min; CD8A, 200×, incubation at RT for 30 min; TIM3, 200×, incubation at RT for 30 min; KLRB1, 100×, incubation at RT for 30 min), with each cycle involving incubation of Horseradish Peroxidase (HRP)-conjugated secondary antibodies followed by tyramide-based fluorescent signal amplification (TSA). Microwave-induced epitope retrieval (PanCK, retrieval with EDTA; CD8A, retrieval with EDTA; TIM3, retrieval with EDTA; KLRB1, retrieval with EDTA) was systematically performed between successive TSA cycles to eliminate antibody cross-reactivity. Following completion of all protein marker labeling, nuclear visualization was achieved through counterstaining with DAPI (4′,6-diamidino-2-phenylindole, Sigma-Aldrich).

Immunohistochemistry

Formalin-fixed, paraffin-embedded tumor sections from patients with MSS CRC were deparaffinized and rehydrated. Antigen retrieval was performed using EDTA buffer (pH 8.0) at 100°C for 15 min in a dedicated retrieval apparatus. Endogenous peroxidase activity was blocked with 3% hydrogen peroxide in methanol for 25 min at RT in the dark. Sections were then blocked with 3% bovine serum albumin for 30min at RT and incubated overnight at 4°C with a mouse monoclonal antibody against CD8α (clone not specified, Servicebio, GB12068, dilution 1:1500). After washing, sections were incubated with a horseradish peroxidase-conjugated goat anti-mouse polymer (S-vision, Servicebio, G1301, ready-to-use) for 50 min at RT. Antibody binding was visualized using a 3,3'-Diaminobenzidine (DAB) chromogen kit, and sections were counterstained with hematoxylin, dehydrated, cleared and mounted. Images were acquired using a digital slide scanner.

DNA constructs and lentivirus production

The Flag-KLRB1 and HA-CLEC2B vectors were constructed by cloning mouse Klrb1 and Clec2b cDNA into the pCHN1 vector or PRK5 vector, respectively. Two shRNA fragments targeting the CDS of mouse *Klrb1* were cloned into the plasmid pLKO.1-TRC (Addgene 10878) as described in the TRC protocols http://www.broadinstitute.org.

Lentiviral transduction

293T cells were co-transfected with the plasmids together with lentivirus-packaging vectors pMD2.G (Addgene 12259) and psPAX2 (Addgene 12260). 48–72 hours after transfection, the culture supernatants containing the released viral particles were collected and added with polybrene (Sigma AL-118) at a final concentration of 8 µg/mL. After 6–10 hours, the media were replaced with fresh viral-free medium to allow further growth until use.

Reverse transcription and RT-qPCR analysis

Total RNA and cDNA were prepared using. Real-time quantitative reverse transcription polymerase chain reaction (RT-qPCR) was performed according to the manufacturer instructions.

Western blot analysis

Cell extracts were separated on 10% sodium dodecyl sulfate-polyacrylamide gel electrophoresis (SDS-PAGE) gels, transferred to PC membranes, blocked with Tris-buffered saline/Tween 20 containing 5% skim milk for 1 hour at RT, and then probed with the indicated primary antibody at 4°C overnight. After three washes, the membranes were incubated with a 1:5,000 dilution of HRP-conjugated secondary antibodies for 1 hour at RT. The immunoblots were detected using enhanced chemiluminescence (ECL).

Flow cytometry

For surface staining, cells were harvested and stained with antibodies at the recommended dilution prior to flow cytometry analysis. For intracellular proteins including cytokines, cells were harvested and washed, fixed with eBioscience IC Fixation Buffer (00–8222-49), permeabilized with eBioscience Permeabilization Buffer (00–8333-56) and stained according to the manufacturer protocol. For intranuclear proteins, cells were harvested and fixed with eBioscience Fixation/Permeabilization Diluent and Concentrate (00–5223-56 and 00–5123-43), permeabilized with eBioscience Permeabilization Buffer (00–8333-56) and stained. Stained cells were washed prior to FACS analysis. BD FACSuite Flow Cytometry Software was used for FACS signal collection. Positive events were determined by isotype control gating for each antibody. Cells were first gated using Forward Scatter (FSC) / Side Scatter (SSC) characteristics to exclude debris, followed by gating Forward Scatter-wight (FSC-W) and Forward Scatter-height (FSC-H), then Side Scatter-weight (SSC-W) and Side Scatter-height (SSC-H) to eliminate non-singlets. Then target cells were gated the population of interest by specific stain. Data analysis was carried out using FlowJo.

Protein expression and purification

After transfection of FLAG-KLRB1 with or not HA-CLEC2B into 293T cells, cells were harvested. The supernatants were incubated with FLAG M2 beads, which were washed three times with wash buffer (PBS, 150 mM NaCl and 1% Triton X-100), followed by competitive elution with FLAG peptides.

Immunoprecipitation assays

Cells were lysed in lysis buffer at 4°C for 20 min. Cell lysates were incubated with Protein A-agarose at 4°C for 2 hours followed by the addition of antibodies overnight at 4°C. The beads were then washed with lysis buffer. The immunoprecipitants were eluted from the beads with 2×SDS loading buffer, separated on 10% SDS-PAGE gels, and immunoblotted with the indicated antibodies.

Statistics and reproducibility

For bioinformatics analysis, group comparisons were analyzed using two-sided unpaired Student's t-test with heteroscedasticity with statistical significance defined as NS (not significant) $p \geq 0.05$, *$p < 0.05$, **$p < 0.01$, ***$p < 0.001$. For experimental data analysis, quantitative measurements, displayed as mean±SD, originated from at least triplicate biological replicates. We performed Shapiro-Wilk normality tests on all experimental data to assess whether they followed a normal distribution. For normally distributed data, we used a two-sided unpaired Student's t-test with heteroscedasticity; for non-normally distributed data, we used the Wilcoxon test. Statistical significance was defined as NS (not significant) for $p \geq 0.05$, *$p < 0.05$, **$p < 0.01$, and ***$p < 0.001$. All raw data points are displayed in graphical representations. Experiments were designed with 3–10 replicates per independent group or condition. The biological duplicates and statistical analyses are provided in the figure legends. Sample sizes were not predetermined using statistical methods but align with commonly adopted parameters in comparable studies. No experimental data were omitted during statistical evaluations. In the absence of specific statements, the experiments were conducted without randomization, and the researchers were aware of the allocation during both the experiments and the outcome assessment. Investigators remained masked to group assignments throughout animal experimentation data recording, non-animal experimental procedures, and analytical evaluations. Minimum cohort size ($n \geq 5$) of animal was based on feasibility and specimen accessibility to validate findings.

Resource availability

Lead contact

For additional details or resource inquiries, please contact the corresponding author, J.C. jiecheng2024@hust.edu.cn.

Materials availability

No novel reagents were synthesized in this study.

Data and code availability

Raw scRNA-seq data of this study can be downloaded at Genome Sequence Archive (GSA)[76 77] for Human Database (https://ngdc.cncb.ac.cn/gsa-human) with accession

number PRJCA062557 and processed data were uploaded to Zenodo with accession number 19638700. Public spatial transcriptome datasets[63 67–69] are available at DNA Data Bank of Japan under accession number E-GEAD-579, https://doi.org/10.5281/zenodo.7551712, Gene Expression Omnibus (GEO) under accession number GSE225857 and http://www.cancerdiversity.asia/scCRLM. Public MSS CRC scRNA-seq dataset[60] was obtained from GEO under accession number GSE132465 and GSE144735. MMRp and MMRd CRC scRNA-seq data[19] were retrieved via figshare at https://doi.org/10.6084/m9.figshare.25323397. Public pan-cancer T-cell scRNA-seq dataset and bulk RNA-seq dataset[78] were downloaded from https://zenodo.org/records/5461803. Public ICB-response information of pan-cancer[79] was obtained from https://zenodo.org/records/11186449. Public ICB treatment scRNA-seq datasets[80–86] were available in GEO (GSE236581, GSE235863, GSE169246, GSE200996 and GSE246613) and http://120.46.71.14/Download.html. Public bulk RNA-seq datasets used for survival analysis were obtained from cBioPortal for Cancer Genomics.[87]

This study employed established analytical methods without novel algorithm development. The R and Python code supporting key analyses is available on request to the corresponding author.

Author affiliations
[1]Department of Pathology, School of Basic Medicine, Tongji Medical College and State Key Laboratory for Diagnosis and Treatment of Severe Zoonotic Infectious Diseases, Huazhong University of Science and Technology, Wuhan, Hubei, China
[2]Institute of Pathology, Tongji Hospital, Huazhong University of Science and Technology, Wuhan, Hubei, China
[3]Department of Gastrointestinal Surgery, Peking University Shougang Hospital, Beijing, China
[4]Center for Precision Diagnosis and Treatment of Colorectal Cancer and Inflammatory Diseases, Peking University Health Science Center, Beijing, China
[5]State Key Laboratory of Molecular Oncology, School of Life Sciences, Tsinghua-Peking Center for Life Sciences, Tsinghua University, Beijing, China
[6]Key Laboratory of Carcinogenesis and Translational Research (Ministry of Education), Department of Unit III of Gastrointestinal Cancer Centre, Peking University Cancer Hospital and Institute, Haidian District Beijing, China
[7]School of Life Sciences, Center for Statistical Science, Peking University, Beijing, China
[8]State Key Laboratory of Natural and Biomimetic Drugs, Beijing, China
[9]National "111" Center for Cellular Regulation and Molecular Pharmaceutics (Ministry of Education), Hubei University of Technology, Wuhan, China
[10]Peking University International Cancer Institute, Peking University, Beijing, China
[11]Peking-Tsinghua Center for Life Sciences, Peking University, Beijing, China
[12]Key Laboratory of Carcinogenesis and Translational Research (Ministry of Education/Beijing), Department of Gastrointestinal Surgery, Peking University Cancer Hospital & Institute, Beijing, China

Acknowledgements We thank Prof. Cheng Li for providing computational resources; Prof. Peng Jiang for discussion; Prof. Dengbo Ji for providing MSS CRC cell line; Zai Chang and the Animal Facility of Tsinghua University for help with mouse care and surgery; Yan Liu and the Tsinghua University Branch of China National Center for Protein Sciences (Beijing) and Tsinghua University Technology Center for Flow cytometry support. Part of bioinformatics data analysis was performed on the High Performance Computing Platform of the Center for Life Sciences, Peking University. This research was supported by National Science and Technology Major Project of the Ministry of Science and Technology of China (2025ZD0549900) and the National Natural Science Foundation of China (82403315) to J.C. This research was supported by Beijing Hospitals Authority Youth Programme (QML20231112) to P.C. This work was supported by Capital's Funds for Health Improvement and Research (CFH 2024-1-6041) and the National Key R&D Program of China (Grant No.2023YFC3402203) to J.G. This work was supported by 2025 High-level Innovation and Entrepreneurship Talent Plan – Dengfeng Program – Young Seedling & Spring Bud Project (G202511076) to M.L.

Contributors J.C. conceived the experimental design. Z.G. and P.C. collected patient samples and performed clinical analysis with the supervision of M.L. and J.G. J.L. performed bioinformatics analyses with the supervision of J.C. J.C. and Y.X. performed experiments with the supervision of J.C. M.Z. helped with IHC experiments. D.H. helped with clinical analysis. Z.Z. helped with bioinformatics analyses. X.Z. helped with MS analysis. Y.Z. helped with experiments. J.C. and J.L. wrote the manuscript. J.C., J.G., M.L. and P.J. supervised the research. All authors commented on the manuscript. J.G. is the guarantor of this work.

Funding This research was supported by National Science and Technology Major Project of the Ministry of Science and Technology of China (2025ZD0549900) and the National Natural Science Foundation of China (82403315) to J.C. This research was supported by Beijing Hospitals Authority Youth Programme (QML20231112) to P.C. This work was supported by Capital's Funds for Health Improvement and Research (CFH 2024-1-6041) and the National Key R&D Program of China (Grant No.2023YFC3402203) to J.G. This work was supported by 2025 High-level Innovation and Entrepreneurship Talent Plan – Dengfeng Program – Young Seedling & Spring Bud Project (G202511076) to M.L.

Competing interests JC reported a patent application related to this study. The remaining authors declare no competing interests.

Patient consent for publication Not applicable.

Ethics approval All experimental protocols involving human subjects and biological samples were performed in accordance with the ethical standards established by the Committee of Tsinghua University. The acquisition and use of clinical specimens received explicit authorization from the Ethics Committee at Peking University Shougang Hospital (Approval No. IRBK-2024-033-01), with written consent documentation secured from all donors prior to participation. Regarding animal research, the study design complied with regulations ruled by the Association for Assessment and Accreditation of Laboratory Animal Care International and was formally sanctioned by the Institutional Animal Care and Use Committee (IACUC) at Tsinghua University following rigorous review. Specifically, in murine tumor models, dimensional parameters of neoplasms were strictly maintained within ethical boundaries prescribed by the IACUC, ensuring that tumor volumes remained below the 2 cm^3 threshold throughout the investigation period.

Provenance and peer review Not commissioned; externally peer reviewed.

Data availability statement Data are available in a public, open access repository.

ORCID iDs
Jie Cheng https://orcid.org/0009-0000-8125-2901
Zihao Zhao https://orcid.org/0009-0009-5322-9451

REFERENCES

1 Ganesh K, Stadler ZK, Cercek A, *et al*. Immunotherapy in colorectal cancer: rationale, challenges and potential. *Nat Rev Gastroenterol Hepatol* 2019;16:361–75.
2 Marcus L, Lemery SJ, Keegan P, *et al*. FDA Approval Summary: Pembrolizumab for the Treatment of Microsatellite Instability-High Solid Tumors. *Clin Cancer Res* 2019;25:3753–8.
3 Morad G, Helmink BA, Sharma P, *et al*. Hallmarks of response, resistance, and toxicity to immune checkpoint blockade. *Cell* 2021;184:5309–37.

4 The Cancer Genome Atlas Network. Comprehensive molecular characterization of human colon and rectal cancer. *Nature New Biol* 2012;487:330–7.
5 Westcott PMK, Sacks NJ, Schenkel JM, *et al*. Low neoantigen expression and poor T-cell priming underlie early immune escape in colorectal cancer. *Nat Cancer* 2021;2:1071–85.
6 Kim CG, Jang M, Kim Y, *et al*. VEGF-A drives TOX-dependent T cell exhaustion in anti-PD-1-resistant microsatellite stable colorectal cancers. *Sci Immunol* 2019;4:eaay0555.
7 Kenison JE, Stevens NA, Quintana FJ. Therapeutic induction of antigen-specific immune tolerance. *Nat Rev Immunol* 2024;24:338–57.
8 Sharma P, Goswami S, Raychaudhuri D, *et al*. Immune checkpoint therapy-current perspectives and future directions. *Cell* 2023;186:1652–69.
9 Andrews LP, Yano H, Vignali DAA. Inhibitory receptors and ligands beyond PD-1, PD-L1 and CTLA-4: breakthroughs or backups. *Nat Immunol* 2019;20:1425–34.
10 Pardoll DM. The blockade of immune checkpoints in cancer immunotherapy. *Nat Rev Cancer* 2012;12:252–64.
11 Shi H, Doench JG, Chi H. CRISPR screens for functional interrogation of immunity. *Nat Rev Immunol* 2023;23:363–80.
12 Belk JA, Yao W, Ly N, *et al*. Genome-wide CRISPR screens of T cell exhaustion identify chromatin remodeling factors that limit T cell persistence. *Cancer Cell* 2022;40:768–86.
13 Schmidt R, Steinhart Z, Layeghi M, *et al*. CRISPR activation and interference screens decode stimulation responses in primary human T cells. *Science* 2022;375:eabj4008.
14 Wu B, Zhang B, Li B, *et al*. Cold and hot tumors: from molecular mechanisms to targeted therapy. *Signal Transduct Target Ther* 2024;9:274.
15 Mellman I, Chen DS, Powles T, *et al*. The cancer-immunity cycle: Indication, genotype, and immunotype. *Immunity* 2023;56:2188–205.
16 Zhang L, Yu X, Zheng L, *et al*. Lineage tracking reveals dynamic relationships of T cells in colorectal cancer. *Nature New Biol* 2018;564:268–72.
17 Kleshchevnikov V, Shmatko A, Dann E, *et al*. Cell2location maps fine-grained cell types in spatial transcriptomics. *Nat Biotechnol* 2022;40:661–71.
18 Wu SZ, Al-Eryani G, Roden DL, *et al*. A single-cell and spatially resolved atlas of human breast cancers. *Nat Genet* 2021;53:1334–47.
19 Chu X, Li X, Zhang Y, *et al*. Integrative single-cell analysis of human colorectal cancer reveals patient stratification with distinct immune evasion mechanisms. *Nat Cancer* 2024;5:1409–26.
20 Vignali DAA, Collison LW, Workman CJ. How regulatory T cells work. *Nat Rev Immunol* 2008;8:523–32.
21 Revel M, Sautès-Fridman C, Fridman W-H, *et al*. C1q+ macrophages: passengers or drivers of cancer progression. *Trends Cancer* 2022;8:517–26.
22 Yi F-S, Qiao X, Dong S-F, *et al*. Complement C1q is a key player in tumor-associated macrophage-mediated $CD8^+$ T cell and NK cell dysfunction in malignant pleural effusion. *Int J Biol Sci* 2024;20:5979–98.
23 Jin S, Plikus MV, Nie Q. CellChat for systematic analysis of cell-cell communication from single-cell transcriptomics. *Nat Protoc* 2025;20:180–219.
24 Launonen I-M, Niemiec I, Hincapié-Otero M, *et al*. Chemotherapy induces myeloid-driven spatially confined T cell exhaustion in ovarian cancer. *Cancer Cell* 2024;42:2045–63.
25 Ho DW-H, Tsui Y-M, Chan L-K, *et al*. Single-cell RNA sequencing shows the immunosuppressive landscape and tumor heterogeneity of HBV-associated hepatocellular carcinoma. *Nat Commun* 2021;12:3684.
26 Moon J, Oh YM, Ha S-J. Perspectives on immune checkpoint ligands: expression, regulation, and clinical implications. *BMB Rep* 2021;54:403–12.
27 Martín P, Blanco-Domínguez R, Sánchez-Díaz R. Novel human immunomodulatory T cell receptors and their double-edged potential in autoimmunity, cardiovascular disease and cancer. *Cell Mol Immunol* 2021;18:919–35.
28 Zhai Y, Moosavi R, Chen M. Immune Checkpoints, a Novel Class of Therapeutic Targets for Autoimmune Diseases. *Front Immunol* 2021;12:645699.
29 Mathewson ND, Ashenberg O, Tirosh I, *et al*. Inhibitory CD161 receptor identified in glioma-infiltrating T cells by single-cell analysis. *Cell* 2021;184:1281–98.
30 Getu AA, Tigabu A, Zhou M, *et al*. New frontiers in immune checkpoint B7-H3 (CD276) research and drug development. *Mol Cancer* 2023;22:43.
31 Nakandakari-Higa S, Walker S, Canesso MCC, *et al*. Universal recording of immune cell interactions in vivo. *Nature New Biol* 2024;627:399–406.
32 Efremova M, Vento-Tormo M, Teichmann SA, *et al*. CellPhoneDB: inferring cell-cell communication from combined expression of multi-subunit ligand-receptor complexes. *Nat Protoc* 2020;15:1484–506.
33 Overman MJ, Kopetz S, McDermott RS, *et al*. Nivolumab ± ipilimumab in treatment (tx) of patients (pts) with metastatic colorectal cancer (mCRC) with and without high microsatellite instability (MSI-H): CheckMate-142 interim results. *JCO* 2016;34:3501.
34 Kirkham CL, Carlyle JR. Complexity and Diversity of the NKR-P1:Clr (Klrb1:Clec2) Recognition Systems. *Front Immunol* 2014;5:214.
35 Cheng J, Xiao Y, Peng T, *et al*. ETV7 limits the antiviral and antitumor efficacy of $CD8^+$ T cells by diverting their fate toward exhaustion. *Nat Cancer* 2025;6:338–56.
36 Pozo D, Valés-Gómez M, Mavaddat N, *et al*. CD161 (human NKR-P1A) signaling in NK cells involves the activation of acid sphingomyelinase. *J Immunol* 2006;176:2397–406.
37 Hwang J-R, Byeon Y, Kim D, *et al*. Recent insights of T cell receptor-mediated signaling pathways for T cell activation and development. *Exp Mol Med* 2020;52:750–61.
38 Johansen KH, Golec DP, Huang B, *et al*. A CRISPR screen targeting PI3K effectors identifies RASA3 as a negative regulator of LFA-1-mediated adhesion in T cells. *Sci Signal* 2022;15:eabl9169.
39 Wang D, Yang L, Yu W, *et al*. Colorectal cancer cell-derived CCL20 recruits regulatory T cells to promote chemoresistance via FOXO1/CEBPB/NF-κB signaling. *j immunotherapy cancer* 2019;7:215.
40 Kurioka A, Cosgrove C, Simoni Y, *et al*. CD161 Defines a Functionally Distinct Subset of Pro-Inflammatory Natural Killer Cells. *Front Immunol* 2018;9:486.
41 Mustelin T, Vang T, Bottini N. Protein tyrosine phosphatases and the immune response. *Nat Rev Immunol* 2005;5:43–57.
42 Ravetch JV, Lanier LL. Immune inhibitory receptors. *Science* 2000;290:84–9.
43 Fergusson JR, Fleming VM, Klenerman P. CD161-expressing human T cells. *Front Immunol* 2011;2:36.
44 Fergusson JR, Smith KE, Fleming VM, *et al*. CD161 defines a transcriptional and functional phenotype across distinct human T cell lineages. *Cell Rep* 2014;9:1075–88.
45 Karunathilaka A, Halstrom S, Price P, *et al*. CD161 expression defines new human γδ T cell subsets. *Immun Ageing* 2022;19:11.
46 Le Bourhis L, Mburu YK, Lantz O. MAIT cells, surveyors of a new class of antigen: development and functions. *Curr Opin Immunol* 2013;25:174–80.
47 Josien R, Heslan M, Soulillou JP, *et al*. Rat spleen dendritic cells express natural killer cell receptor protein 1 (NKR-P1) and have cytotoxic activity to select targets via a Ca2+-dependent mechanism. *J Exp Med* 1997;186:467–72.
48 Aldemir H, Prod'homme V, Dumaurier M-J, *et al*. Cutting edge: lectin-like transcript 1 is a ligand for the CD161 receptor. *J Immunol* 2005;175:7791–5.
49 Rosen DB, Bettadapura J, Alsharifi M, *et al*. Cutting edge: lectin-like transcript-1 is a ligand for the inhibitory human NKR-P1A receptor. *J Immunol* 2005;175:7796–9.
50 Xu N, Meng X, Chu H, *et al*. The prognostic significance of KLRB1 and its further association with immune cells in breast cancer. *PeerJ* 2023;11:e15654.
51 Liu X, Cui Q, Qin N. Low expression of KLRB1 predicts poor survival outcomes and is associated with immune infiltration in breast cancer. *Transl Cancer Res* 2024;13:1225–40.
52 Huang G, Xiao S, Jiang Z, *et al*. Machine learning immune-related gene based on KLRB1 model for predicting the prognosis and immune cell infiltration of breast cancer. *Front Endocrinol* 2023;14:1185799.
53 Liang C, Chen Y, Chen S, *et al*. KLRB1 is a novel prognostic biomarker in endometrial cancer and is associated with immune infiltration. *Transl Cancer Res* 2023;12:3641–52.
54 Chen J-L, Wu C-Y, Luo X-Y, *et al*. Down-regulation of KLRB1 is associated with increased cell growth, metastasis, poor prognosis, as well as a dysfunctional immune microenvironment in LUAD. *Sci Rep* 2024;14:11782.
55 Xu S, Xu Y, Chai W, *et al*. KLRB1 expression is associated with lung adenocarcinoma prognosis and immune infiltration and regulates lung adenocarcinoma cell proliferation and metastasis through the MAPK/ERK pathway. *J Thorac Dis* 2024;16:3764–81.
56 Fang S, Zhou Y. Deciphering the role of KLRB1: a novel prognostic indicator in hepatocellular carcinoma. *BMC Gastroenterol* 2024;24:210.

57 Wang J, Wang X, Shi J, *et al*. CD161, a promising prognostic biomarker in hepatocellular carcinoma, correlates with immune infiltration. *PeerJ* 2025;13:e19055.
58 Sun Y, Wu L, Zhong Y, *et al*. Single-cell landscape of the ecosystem in early-relapse hepatocellular carcinoma. *Cell* 2021;184:404–21.
59 Hao Y, Stuart T, Kowalski MH, *et al*. Dictionary learning for integrative, multimodal and scalable single-cell analysis. *Nat Biotechnol* 2024;42:293–304.
60 Lee H-O, Hong Y, Etlioglu HE, *et al*. Lineage-dependent gene expression programs influence the immune landscape of colorectal cancer. *Nat Genet* 2020;52:594–603.
61 Qi J, Sun H, Zhang Y, *et al*. Single-cell and spatial analysis reveal interaction of FAP+ fibroblasts and SPP1+ macrophages in colorectal cancer. *Nat Commun* 2022;13:1742.
62 Zheng X, Song J, Yu C, *et al*. Single-cell transcriptomic profiling unravels the adenoma-initiation role of protein tyrosine kinases during colorectal tumorigenesis. *Sig Transduct Target Ther* 2022;7:60.
63 Wu Y, Yang S, Ma J, *et al*. Spatiotemporal Immune Landscape of Colorectal Cancer Liver Metastasis at Single-Cell Level. *Cancer Discov* 2022;12:134–53.
64 Li J, Wu C, Hu H, *et al*. Remodeling of the immune and stromal cell compartment by PD-1 blockade in mismatch repair-deficient colorectal cancer. *Cancer Cell* 2023;41:1152–69.
65 Zheng X, Song J, Yu C, *et al*. Single-cell transcriptomic profiling unravels the adenoma-initiation role of protein tyrosine kinases during colorectal tumorigenesis. *Signal Transduct Target Ther* 2022;7:60.
66 Qiu X, Mao Q, Tang Y, *et al*. Reversed graph embedding resolves complex single-cell trajectories. *Nat Methods* 2017;14:979–82.
67 Valdeolivas A, Amberg B, Giroud N, *et al*. Profiling the heterogeneity of colorectal cancer consensus molecular subtypes using spatial transcriptomics. *NPJ Precis Oncol* 2024;8:10.
68 Wang F, Long J, Li L, *et al*. Single-cell and spatial transcriptome analysis reveals the cellular heterogeneity of liver metastatic colorectal cancer. *Sci Adv* 2023;9:eadf5464.
69 Ozato Y, Kojima Y, Kobayashi Y, *et al*. Spatial and single-cell transcriptomics decipher the cellular environment containing HLA-G+ cancer cells and SPP1+ macrophages in colorectal cancer. *Cell Rep* 2023;42:111929.
70 Seo M-K, Kang H, Kim S. Tumor microenvironment-aware, single-transcriptome prediction of microsatellite instability in colorectal cancer using meta-analysis. *Sci Rep* 2022;12:6283.
71 Zhang W, Sloan-Lancaster J, Kitchen J, *et al*. LAT: the ZAP-70 tyrosine kinase substrate that links T cell receptor to cellular activation. *Cell* 1998;92:83–92.
72 Gonen R, Beach D, Ainey C, *et al*. T Cell Receptor-induced Activation of Phospholipase C-γ1 Depends on a Sequence-independent Function of the P-I Region of SLP-76. *Journal of Biological Chemistry* 2005;280:8364–70.
73 Park Y-J, Yoo S-A, Kim M, *et al*. The Role of Calcium–Calcineurin–NFAT Signaling Pathway in Health and Autoimmune Diseases. *Front Immunol* 2020;11:195.
74 Xu S, Hu E, Cai Y, *et al*. Using clusterProfiler to characterize multiomics data. *Nat Protoc* 2024;19:3292–320.
75 Aibar S, González-Blas CB, Moerman T, *et al*. SCENIC: single-cell regulatory network inference and clustering. *Nat Methods* 2017;14:1083–6.
76 Xue Y, Bao Y, Zhang Z, *et al*. Database Resources of the National Genomics Data Center, China National Center for Bioinformation in 2022. *Nucleic Acids Res* 2022;50:D27–38.
77 Chen T, Chen X, Zhang S, *et al*. The Genome Sequence Archive Family: Toward Explosive Data Growth and Diverse Data Types. *Genomics Proteomics Bioinformatics* 2021;19:578–83.
78 Zheng L, Qin S, Si W, *et al*. Pan-cancer single-cell landscape of tumor-infiltrating T cells. *Science* 2021;374:abe6474.
79 Chang T-G, Cao Y, Sfreddo HJ, *et al*. LORIS robustly predicts patient outcomes with immune checkpoint blockade therapy using common clinical, pathologic and genomic features. *Nat Cancer* 2024;5:1158–75.
80 Chen Y, Wang D, Li Y, *et al*. Spatiotemporal single-cell analysis decodes cellular dynamics underlying different responses to immunotherapy in colorectal cancer. *Cancer Cell* 2024;42:1268–85.
81 Franken A, Bila M, Mechels A, *et al*. $CD4^+$ T cell activation distinguishes response to anti-PD-L1+anti-CTLA4 therapy from anti-PD-L1 monotherapy. *Immunity* 2024;57:541–58.
82 Guo X, Nie H, Zhang W, *et al*. Contrasting cytotoxic and regulatory T cell responses underlying distinct clinical outcomes to anti-PD-1 plus lenvatinib therapy in cancer. *Cancer Cell* 2025;43:248–68.
83 Zhang Y, Chen H, Mo H, *et al*. Single-cell analyses reveal key immune cell subsets associated with response to PD-L1 blockade in triple-negative breast cancer. *Cancer Cell* 2021;39:1578–93.
84 Luoma AM, Suo S, Wang Y, *et al*. Tissue-resident memory and circulating T cells are early responders to pre-surgical cancer immunotherapy. *Cell* 2022;185:2918–35.
85 Shiao SL, Gouin KH 3rd, Ing N, *et al*. Single-cell and spatial profiling identify three response trajectories to pembrolizumab and radiation therapy in triple negative breast cancer. *Cancer Cell* 2024;42:70–84.
86 Bassez A, Vos H, Van Dyck L, *et al*. A single-cell map of intratumoral changes during anti-PD1 treatment of patients with breast cancer. *Nat Med* 2021;27:820–32.
87 Cerami E, Gao J, Dogrusoz U, *et al*. The cBio cancer genomics portal: an open platform for exploring multidimensional cancer genomics data. *Cancer Discov* 2012;2:401–4.
88 Jiang S, Li H, Zhang L, *et al*. Generic Diagramming Platform (GDP): a comprehensive database of high-quality biomedical graphics. *Nucleic Acids Res* 2025;53:D1670–6.